Atmos. Chem. Phys. Discuss., 12, 9377–9450, 2012
www.atmos-chem-phys-discuss.net/12/9377/2012/
doi:10.5194/acpd-12-9377-2012

Atmospheric
Chemistry
and Physics
Discussions

An analysis of fast photochemistry over high northern latitudes during spring and summer using in-situ observations from ARCTAS and TOPSE

J. R. Olson[1], J. H. Crawford[1], W. Brune[2], J. Mao[3], X. Ren[4], A. Fried[5,*], B. Anderson[1], E. Apel[5], M. Beaver[6,], D. Blake[7], G. Chen[1], J. Crounse[6], J. Dibb[8], G. Diskin[1], S. R. Hall[5], L. G. Huey[9], D. Knapp[5], D. Richter[5], D. Riemer[10], J. St. Clair[6], K. Ullmann[5], J. Walega[5], P. Weibring[5], A. Weinheimer[5], P. Wennberg[6], and A. Wisthaler[11,***]**

[1]NASA Langley Research Center, Hampton, VA, USA
[2]Penn State, University Park, PA, USA
[3]Princeton University, Princeton, NJ, USA
[4]NOAA Air Resources Laboratory, Silver Spring, MD, USA
[5]NCAR, Boulder, CO, USA
[6]California Institute of Technology, Pasadena, CA, USA
[7]University of California, Irvine, CA, USA
[8]University of New Hampshire, Durham, NH, USA

Title Page
Abstract | Introduction
Conclusions | References
Tables | Figures
◀| | ▶|
◀ | ▶
Back | Close
Full Screen / Esc
Printer-friendly Version
Interactive Discussion

[9] Georgia Institute of Technology, Atlanta, GA, USA
[10] University of Miami, Miami, FL, USA
[11] University of Innsbruck, Innsbruck, Austria
[*] now at: INSTARR, University of Colorado, Boulder, CO, USA
[**] now at: Environmental Protection Agency, Research Triangle Park, NC, USA
[***] now at: Norwegian Institute of Air Research, Kjeller, Norway

Received: 12 March 2012 – Accepted: 27 March 2012 – Published: 11 April 2012

Correspondence to: J. R. Olson (jennifer.r.olson@nasa.gov)

Published by Copernicus Publications on behalf of the European Geosciences Union.

Abstract

Observations of chemical constituents and meteorological quantities obtained during the two Arctic phases of the airborne campaign ARCTAS (Arctic Research of the Composition of the Troposphere from Aircraft and Satellites) are analyzed using an observationally constrained steady state box model. Measurements of OH and HO_2 from the Penn State ATHOS instrument are compared to model predictions. Forty percent of OH measurements below 2 km are at the limit of detection during the spring phase (ARCTAS-A). While the median observed-to-calculated ratio is near one, both the scatter of observations and the model uncertainty for OH are at the magnitude of ambient values. During the summer phase (ARCTAS-B), model predictions of OH are biased low relative to observations and demonstrate a high sensitivity to the level of uncertainty in NO observations. Predictions of HO_2 using observed CH_2O and H_2O_2 as model constraints are up to a factor of two larger than observed. A temperature-dependent terminal loss rate of HO_2 to aerosol recently proposed in the literature is shown to be insufficient to reconcile these differences. A comparison of ARCTAS-A to the high latitude springtime portion of the 2000 TOPSE campaign (Tropospheric Ozone Production about the Spring Equinox) shows similar meteorological and chemical environments with the exception of peroxides; observations of H_2O_2 during ARCTAS-A were 2.5 to 3 times larger than those during TOPSE. The cause of this difference in peroxides remains unresolved and has important implications for the Arctic HO_x budget. Unconstrained model predictions for both phases indicate photochemistry alone is unable to simultaneously sustain observed levels of CH_2O and H_2O_2; however when the model is constrained with observed CH_2O, H_2O_2 predictions from a range of rainout parameterizations bracket its observations. A mechanism suitable to explain observed concentrations of CH_2O is uncertain. Free tropospheric observations of acetaldehyde (CH_3CHO) are 2–3 times larger than its predictions, though constraint of the model to those observations is sufficient to account for less than half of the deficit in predicted CH_2O. The box model calculates gross O_3 formation during spring to maximize from

1–4 km at 0.8 ppbv d^{-1}, in agreement with estimates from TOPSE, and a gross production of 2–4 ppbv d^{-1} in the boundary layer and upper troposphere during summer. Use of the lower observed levels of HO_2 in place of model predictions decreases the gross production by 25–50 %. Net O_3 production is near zero throughout the ARCTAS-A troposphere, and is 1–2 ppbv in the boundary layer and upper altitudes during ARCTAS-B.

1 Introduction

The climate of the Arctic environment is changing more rapidly than any other region. While polar temperature trends vary, the overall trend is one of substantial warming (Arctic Climate Impact Assessment, http://amap.no/acia/), and the September sea ice extent is decreasing at accelerating rates (Lemke et al., 2007; Comiso et al., 2008). Studies indicate that regional radiative forcing from aerosols and tropospheric O_3 is likely to be a significant contributor to the Arctic warming trend during the winter and spring, and that factors controlling these constituents in the Arctic are poorly understood and simulated (Stohl, 2006; Law and Stohl, 2007; Shindell et al., 2007; Quinn et al., 2008).

A major mechanism for long-range transport of O_3, aerosols and other pollutants into high latitudes is the near-surface transport of pollution from northern Euro-Asian sources into the wintertime Arctic (the "Arctic haze" phenomenon; e.g., Radke et al., 1984; Brock et al., 1989; Shaw, 1995). Recent studies have expanded upon that understanding to show that transport of middle latitude pollutants into the Arctic can occur throughout the extent of the Arctic troposphere at various times throughout the year, from source regions located in Asia, Europe and North America (Stohl, 2006; Shindell et al., 2008; Singh et al., 2010; Fisher et al., 2010). Additionally, emissions from high latitude boreal forest fires over North America and Asia are transported into the Arctic predominantly during summer, but evidence of long range transport from fires is found during spring as well (Scheuer et al., 2003; Singh et al., 2010).

O_3 photochemistry at high latitudes is impacted by several unique characteristics: extreme cold and dry conditions and long seasonal periods of darkness followed by long periods of sunlight at high solar zenith angles. The persistent snow and sea ice surface increases incident radiation due to a heightened surface albedo, and photochemical reactions within the snowpack itself result in emissions of gases such as hydrogen peroxide (H_2O_2), formaldehyde (CH_2O), and HONO, which can impact near-surface HO_x chemistry (Chen et al., 2004; Frey et al., 2009). During spring, enhanced concentrations of gaseous bromine radicals (BrO) are frequently observed over Arctic sea ice upon polar sunrise. The catalytic cycling of these halogen radicals has been implicated as the cause of local scale near-complete destruction of surface O_3 and further, they influence the cycling and photochemistry of HO_x, NO_x, and O_3 (e.g., Barrie et al., 1988; Evans et al., 2003, McElroy et al., 1999; von Glasgow et al., 2004). Studies stemming from the 2000 TOPSE aircraft campaign (Tropospheric Ozone Production about the Spring Equinox) highlight the importance of photochemistry at high latitudes, suggesting that gross photochemical O_3 formation is equal to or greater than the source from long range transport throughout the spring in the free troposphere, and is greater than transport sources at surface altitudes after March (Stroud et al., 2004; Emmons et al., 2003).

This study examines fast photochemistry from the perspective of in-situ data and model analysis during the high latitude spring and summer, including radical budgets and cycling, and O_3 production and destruction. The data are from NASA's 2008 ARCTAS (Arctic Research of the Composition of the Troposphere from Aircraft and Satellites) campaign, and data from springtime high latitudes from portions of the TOPSE campaign are compared to ARCTAS.

2 Data and modeling approach

2.1 Campaign deployments

2.1.1 ARCTAS

The high-latitude portion of ARCTAS was comprised of two deployment phases during spring and summer of 2008 and utilized three aircraft: the NASA DC-8, P-3B and B-200. The DC-8 instrumentation provided a suite of measurements of species related to aerosol and tropospheric O_3 chemistry, pollution sources, and radical chemistry. A more complete description of the aircraft payload is in Jacob et al. (2010).

The spring deployment phase (ARCTAS-A) was based out of Fairbanks, Alaska (65° N, 148° W) from 1–19 April, during which the DC-8 flew 9 sorties across the Arctic between Alaska, Thule Greenland, and Iqaluit Canada (see Fig. 1 for DC-8 flight paths during ARCTAS). The summer phase (ARCTAS-B) was based out of Cold Lake, Edmonton Canada (54° N, 110° W) from 26 June–14 July, with 9 sorties ranging across Canada and up to Thule and Summit in Greenland. A third phase (ARCTAS-CARB) took place immediately prior to ARCTAS-B in coordination with the California Air Resources Board (CARB), and was focused on middle latitude pollution off the coast of California to improve state emission inventories for greenhouse gases and aerosols. The weight of analysis for this high latitude study is on ARCTAS-A and -B.

2.1.2 TOPSE

During 2000, NCAR (National Center for Atmospheric Research) sponsored the airborne experiment TOPSE (Tropospheric Ozone Production about the Spring Equinox); it was conducted using an instrumented C-130 aircraft from February–May 2000, which brackets the seasonal period covered by ARCTAS-A. The geographical extent of the campaign included middle and high latitudes over North America (40°–85° N) (Atlas et al., 2003). The high latitude data covered a relatively narrow longitude range over

Central to Eastern Canada and up to Thule, Greenland, meaning most data was obtained further to the east over the North American high latitudes and nearly a decade earlier than during ARCTAS-A (See Fig. 1). Nevertheless, it is reasonable to compare data obtained within the high latitude air masses during these two campaigns. Here, the subset of the TOPSE data obtained during March and April at latitudes north of 50° N is considered (herein called TOPSE-sp).

2.2 Box model

The NASA Langley Research Center photochemical box model (LaRC-V08) (Crawford et al., 1999; Olson et al., 2006) uses a diurnal steady state approach with long-lived species constrained to measurements. Reactions and rates for basic HO_x-NO_x-CH_4-CO chemistry are those recommended by Sander et al. (2006) and Atkinson et al. (2006). Non-methane hydrocarbon (NMHC) chemistry is originally based on the lumped scheme from Lurmann et al. (1986), with adjustments as discussed in the appendix of Crawford et al. (1999). Because halogen chemistry is expected to impact surface O_3 chemistry and radical cycling near the surface and in the lower troposphere the box model is updated to include bromine photochemistry (see Table 1).

As in previous studies, photolysis rate coefficients are based on in-situ measurements (Shetter and Muller, 1999). A DISORT four-stream implementation of the NCAR Tropospheric Ultraviolet Visible (TUV) radiative transfer code is first used to calculate the diurnal variation of photolysis rates for clear-sky conditions (Madronich and Flocke, 1998). To adjust these clear-sky rates to account for local cloudiness and surface reflectance, a normalization factor is applied so that observed rates at the time of observation are matched. In the event that a given radical precursor is not constrained to observations, surface deposition and rainout for soluble species are parameterized as in Logan et al. (1981), i.e., for altitudes < 1 km, a surface deposition loss rate of $1 \times^{-5}$ s^{-1} is assigned to most species impacted by surface deposition, with a smaller loss rate of 0.3×10^{-5} s^{-1} for CH_3OOH. Above the boundary layer, the rainout parameterization assumes a 5 day lifetime for altitudes up to 4 km, with an exponentially decreasing loss rate above. Aerosol and cloud uptake for HO_2 is not directly computed in the base simulation but potential impacts of heterogeneous loss in the high latitude environment (e.g., Mao et al., 2010) are explored.

Model calculations require constraint to observations of temperature, pressure, H_2O, O_3, CO, NO, CH_4, NMHCs, ketones (acetone and MEK), and alcohols (methanol and ethanol). In addition to these minimum requirements, several additional constraints may be incorporated if desired when measurements are available; these include CH_2O, H_2O_2 and CH_3OOH, nitric acid (HNO_3), peroxy acetyl nitrate (PAN), and BrO. Constraining parameters are held constant throughout the diurnal cycle with the exception of NO. The total short-lived nitrogen ($NO+NO_2+NO_3+2N_2O_5+HONO+HNO_4$) is held constant, with partitioning into the individual species calculated by the model throughout the day. The sum total of short-lived nitrogen is determined when NO matches the observed value at the time of measurement. All model-calculated species are integrated to find a reproducible diurnal cycle within a given tolerance.

The modeled data points are obtained from data merges averaged to a 1 min timeline. There are occasions when pronounced heterogeneity of 1 Hz NO measurements within the 1 min time span can result in erroneous model predictions of HO_x and related radical species (Olson et al., 2006). In these cases, the 1 min. average has been broken into 60 one-second points for modeling purposes, using 1 Hz data for NO, O_3, CO and H_2O. The high-resolution model predictions are then averaged back to the 1 min. merge timeline for analysis. The merged data and selected box model results from ARCTAS are available on a public archive (http://www-air.larc.nasa.gov/cgi-bin/arcstat-c).

Sources of uncertainty in model predictions include uncertainties in kinetic and photolytic rate constants, and uncertainties in measurements of constraining observations. Estimates of total model uncertainty are obtained using a Monte Carlo technique and/or a Sensitivity approach. The method for uncertainty estimation for the LaRC box model is described in more detail in Appendix A.

2.3 Data

The data utilized for model constraint and analysis is presented in Table 2. Key measurements for the high latitude HO_x budget include peroxides (H_2O_2 in particular) from the CIT-CIMS (California Institute of Technology – chemical ionization mass spectroscopy) instrument, which has a 2σ uncertainty of 100 pptv + 50 % of the measurement value (Crounse et al., 2006). Formaldehyde is measured using a difference frequency generation (DFG)/absorption spectroscopy technique (Weibring et al., 2007) with a systematic uncertainty at the 2σ level of 12.4 %, and a typical 1 min. LOD (2σ) of 22 pptv with degradation of the LOD to ∼59 pptv during periods of large changes in aircraft cabin pressure (http://www-air.larc.nasa.gov/cgi-bin/arcstat-c). Water vapor is obtained from the NASA Langley Research Center DLH (Diode Laser Hygrometer) system with an uncertainty of 10 % (Diskin et al., 2002). The O_3 and NO measurements are obtained from the NCAR four-channel chemiluminescence instrument (Weinheimer et al., 1994) with an 8 % 2σ uncertainty for O_3 and a 16 pptv 2σ uncertainty for the 60 s average of NO when NO is less than 100 pptv.

Measurements of OH and HO_2 from the Penn State laser induced fluorescence Airborne Tropospheric Hydrogen Oxide Sensor (ATHOS) are available for comparison to model predictions. The HO_x measurements have an uncertainty for both species of ±32 %, and a limit of detection (LOD) of 0.01 pptv for OH and 0.1 pptv for HO_2 (Brune et al., 1999; Faloona et al., 2004). During ARCTAS, the NCAR CIMS instruments also provided measurements of OH and HO_2 (Cantrell et al., 2003b; Mauldin et al., 1999); however due to some irregularities of the inlet heater, the level of coverage from the CIMS instrument was reduced. This analysis uses the ATHOS HO_x measurements. Ren et al. (2012) focuses on a comparison between the two independent measurements of HO_x.

To maximize the total number of points available for modeling, missing data for acetone, methanol, and NMHCs (with the exception of isoprene) are interpolated from adjacent measurements within ±5 min and ±0.5 km. Any remaining missing acetone and methanol are filled using TOGA data (Apel et al., 2003), and where those are unavailable, they are filled using data correlations to CO derived from ARCTAS data. Similarly, missing data for MEK and ethanol are filled using data correlations to acetone or methanol.

A percentage of the reported measurements of NO are negative, particularly during the summer phase: 6 % of the NO is negative during ARCTAS-A and 20 % is negative during ARCTAS-B (see Fig. 2). For modeling purposes, any 1 min. averaged NO less than a threshold value of 1 pptv, including negative values, is set equal to 1 pptv. To test the sensitivity to this choice of minimum threshold, it is varied between 0.1 and 2 pptv. Relative to a 1 pptv threshold, median predictions of OH for these tests vary less than 8 %, and median predictions of HO_2 vary less than 2 %, all of which are less than the relative differences between predictions and measured values at the low NO points. Note that this is not equivalent to estimating the uncertainty in model predictions due to the total uncertainty in NO observations.

Data points identified as stratospherically influenced are removed from this analysis. Points are considered stratospherically influenced when $O_3 > 100$ ppbv while either CO < 100 ppbv or H_2O is < a threshold value (50 ppmv during ARCTAS-A and 100 ppmv during ARCTAS-B). Thirteen percent of the data during ARCTAS-A are identified and removed, and 4 % of the summer data are removed. Because the altitude range of the C-130 used during TOPSE is limited to less than 8 km, instances of stratospheric influence are rare; about 2 % of the TOPSE-sp data are removed, using the same criteria as for ARCTAS-A. In all cases, the latitude range of the considered data is limited to north of 50° N.

3 Meteorological and photochemical background at high latitudes

3.1 Meteorology

During ARCTAS-A, the general location of the Arctic front was 60° N (Fuelberg et al., 2010), and most of the aircraft sampling was well north of that. Therefore most of the data was obtained within the extreme cold and dry air of the Arctic air mass. Springtime values for temperature and moisture at high latitudes during TOPSE-sp were comparable to those during ARCTAS-A (Table 3). Alternately, the median sampled latitude during ARCTAS-B was 57° N, while the Arctic front was located well to the north of the bulk of sampled latitudes during that period, leading to higher temperatures and moisture relative to the spring campaigns.

Table 3 also shows the median observed photolysis rates for NO_2 (J-NO_2) and O_3 (J-O^1D). The near-surface instantaneous observations for J-NO_2 are higher during the spring campaigns (ARCTAS-A and TOPSE-sp) than during summer (ARCTAS-B), while J-O^1D shows the opposite tendency. Neglecting transient influences from cloud and aerosols, photolysis is affected by three primary factors: the range of sampled solar zenith angles (SZA), the surface albedo, and the overhead O_3 column. While the range of SZA during the spring is limited to higher values (lower photolysis rates), the persistent snow and ice cover significantly enhances the surface albedo and increases photolysis rates. This albedo-driven increase during spring dominates the difference in rates for J-NO_2. While J-NO_2 is relatively unaffected by changes in the overhead O_3 column, the larger overhead O_3 column during spring (396 DU) relative to summer (316 DU) suppresses J-O^1D and offsets its increase due to the albedo enhancement.

3.2 Chemical environment

3.2.1 Seasonal comparison

Figures 3–5 show observed profiles of selected species during the spring from ARCTAS-A (dark blue) and from TOPSE-sp (lighter shade of blue). The inner 50th percentile range (25–75 %) within each altitude bin is shown by the colored bars, and the median value is indicated by the vertical lines within the bars. For seasonal comparison, profiles obtained during the summer (ARCTAS-B) are also shown (red).

During ARCTAS-B, there were a number of episodic encounters with fresh biomass burning plumes, and the influence of biomass burning is prevalent to various extents throughout the region. Data points that are clearly within fresh pollution or biomass burning plumes are identified based on at least one of several thresholds being exceeded: CO $>$ 300 ppbv, NO $>$ 500 pptv excluding the upper troposphere, CH_3CN $>$ 300 pptv, or benzene $>$ 150 pptv. Below 2 km, 37 % of the data are identified as fresh plumes (9 % of the data above 2 km). The remaining points represent the "background" shown by the bars in Figs. 3–5. The dashed red line in the figures shows the median profile obtained when all data for ARCTAS-B is used, including that from fresh plumes.

Figure 3a,b reflects the build-up of longer-lived species (e.g., CO and C_3H_8) during winter and early spring. The lifetimes of CO and the NMHC species (Table 4) are dominated by reaction with OH and are 3–4 times longer during spring than summer due to the seasonal variation of OH. Long range transport from middle to high latitudes can be important for these species with lifetimes greater than a few weeks. Fisher et al. (2010) concluded that long-range transport during this time is predominantly from Europe at altitudes near the surface and from Asia throughout the remaining troposphere. Alternately, the dominant impact of local biomass burning emissions during summer (ARCTAS-B) is clearly shown to dominate profiles of the shorter-lived C_2H_4 (Fig. 3c). While middle tropospheric median concentrations of C_2H_4 are similarly low during the two seasons, there is a noticeable increase in the range of values from 2–6 km during ARCTAS-A, and $>$ 8 km during ARCTAS-B. The increased middle tropospheric variability during ARCTAS-A is associated with plumes containing increased CH_3CN, indicating influence from transport of biomass burning emissions, primarily from Asian source regions (Singh et al., 2010; Fisher et al., 2010). During summer, the highest C_2H_4 concentrations at upper altitudes are also associated with higher CH_3CN and CO, consistent with biomass burning pollution. Instances of fast convection of fresh pollution during ARCTAS-B have been identified (e.g., Apel et al., 2012), suggesting that the increased range of values for ethene at upper altitudes during summer is impacted by convection of local biomass burning pollution. O_3 profiles are similar throughout the troposphere during both seasons, with surface values near 30 ppbv increasing to 70 ppbv in the upper troposphere (Fig. 3d). The relatively broad 50th percentile range near the surface during the spring is the result of sampling instances of near-surface halogen-driven O_3 depletion events.

The larger background concentrations and range of NO at low altitudes during ARCTAS-B reflect the pervasive influence from local biomass burning (Fig. 4a). Middle tropospheric concentrations of NO are generally less than 10–20 pptv during both seasons. Browne et al. (2011) determined that both of the NO_2 measurements available during ARCTAS are likely to be contaminated by $CH_3O_2NO_2$ at low temperatures. Therefore, the NO/NO_2 ratio shown in Fig. 4b is computed using observed NO and model predictions of NO_2. The lower summertime ratio near the surface is impacted equally by the lower near surface J-NO_2 during summer relative to spring (Sect. 3.1) and by the larger summertime concentrations of peroxy radicals, which convert NO to NO_2. Measurements of gas phase HNO_3 using the University of New Hampshire mist chamber instrument are shown in Fig. 4c, and indicate similar and consistent concentrations in the upper troposphere of less than 100 pptv. The data show flat altitude profiles during spring, and an increase in concentration near the surface during summer.

Figure 5 shows profiles for HO_x precursor reservoirs H_2O_2, CH_3OOH, H_2O_2/CH_3OOH and CH_2O. The relatively short lifetimes for these species shown in Table 4 suggest that long-range transport is unlikely to have a dominant direct impact on concentrations. Concentrations are larger during ARCTAS-B throughout the full extent of the troposphere, reflecting both increased local emission from biomass burning sources and more vigorous photochemical formation in the background atmosphere during the summer.

In comparing the "background" profiles during ARCTAS-B with those using all data, including fresh pollution plumes (dashed red line), it is clear that median values increase in the lowest few km for CO, NMHCs, NO, CH_3OOH and CH_2O as a result of including pollution plumes. HNO_3 and O_3 concentrations, however, are relatively unaffected. This implies there is little impact on net O_3 production within the biomass burning plumes, consistent with the analysis of Singh et al. (2010).

3.2.2 TOPSE-sp versus ARCTAS-A

The data in Table 3 and Figs. 3–5 indicate that the air masses sampled during ARCTAS-A and TOPSE-sp were highly similar in meteorological and photochemical characteristics, with the exception of peroxides. Median observations for H_2O_2 during ARCTAS-A were 300–450 pptv throughout the free troposphere, which are 2.5 to 3 times higher than those during TOPSE-sp (100–200 pptv). Measurements from the Atmospheric Chemistry Experiment satellite (ACE; Rinsland et al., 2007) suggest a rapid seasonal change of peroxides in the upper Arctic troposphere between March and May, which would create the possibility of a timing bias between ARCTAS-A and TOPSE; however both of the March and the April profiles from TOPSE remain distinctly lower than that from ARCTAS-A (Fig. 6) and the difference between March and April TOPSE data above 4 km is minimal.

If the differences in H_2O_2 between the campaigns are due to a significant difference in rainout history between TOPSE and ARCTAS-A, these differences should also be reflected in other soluble species, notably HNO_3 and to a lesser extent, CH_3OOH. Figure 4c shows slightly lower median values of HNO_3 during TOPSE relative to ARCTAS-A; however, the ambient variability for both campaigns indicated by the 50th percentile ranges is heavily overlapping, while there is a clear separation between peroxide ranges of ambient variability between the two campaigns. Further, a reverse bias is seen for CH_3OOH, with observations during ARCTAS-A being 50–75 % lower than those during TOPSE-sp, which is not supportive of an increased role for rainout during TOPSE. As a result of the different biases for the two peroxides, the H_2O_2/CH_3OOH ratios in the free troposphere are dramatically different for the two spring campaigns, with values of 3–4 during ARCTAS-A, and values near one during TOPSE-sp. The similarity in CO, NO, and NMHC observations during the two spring campaigns precludes a significant difference due to transport source regions. Given the similarities in physical conditions (H_2O, temperature, radiation) and in other species important in the photochemical budget of peroxides (O_3, CO, CH_2O), it is difficult to identify a physical reason that peroxides would show such significant differences between the two campaigns.

H_2O_2 measurements during ARCTAS were obtained from both the single-quad and triple-quad implementations of the CIMS instruments, which use independent calibrations for H_2O_2 determinations (Crounse et al., 2006). The two measurements show a high correlation to each other, with no significant bias. The measurements of peroxides during TOPSE-sp were obtained using the University of Rhode Island's instrument utilizing High Performance Liquid Chromatography (URI-HPLC) (Lee et al., 1995; Snow et al., 2003). Both the URI-HPLC instrument and the CIT-CIMS instruments were onboard the DC-8 during NASA's 2004 INTEX-NA campaign (Singh et al., 2006; Snow et al., 2007), during which the two instruments compared well. The median value of H_2O_2 at altitudes > 6 km during INTEX-A was 337 pptv, within the range of concentrations measured during ARCTAS-A. At these lower-concentrations, the fit of CIT-CIMS data to the URI-HPLC data gives a slope of 0.87 and an intercept of 38 pptv. The median ratio between the two peroxide measurements is 0.98, and the r^2 is 0.85, suggesting no bias between the two instruments during INTEX-NA. The cause of the difference in H_2O_2 of several hundred pptv in the free troposphere during ARCTAS-A and TOPSE-sp is unresolved, and, as will be shown, has important implications for conclusions related to the Arctic HO_x budget.

4 Assessment of HO_x photochemistry

For the purpose of a comparison of HO_x observations during ARCTAS to model predictions, the box model is run with full constraints, including CH_2O. The analysis is limited to the subset of data points that include measurements of the major reservoir HO_x precursors (CH_2O and H_2O_2, discussed in Sect. 4.1). The other constraints (CH_3OOH, PAN and HNO_3) are used when measurements are available. With these restrictions, there are a total of 1928 ATHOS HO_x measurements available for analysis during ARCTAS-A and 2101 during ARCTAS-B.

4.1 HO_x sources

Because of the rapid cycling between OH and HO_2, it is useful to examine the source of the combined radicals ($HO_x = OH + HO_2$). Primary sources of HO_x include O_3 photolysis in the presence of water vapor, the photolysis of ketones (particularly acetone), and ozoneolysis of alkenes. Additionally, HO_x reservoir species such as H_2O_2, CH_3OOH, CH_2O and HO_2NO_2 formed during HO_x cycling are a source of HO_x upon photolysis. The source of HO_x originating from multiple species flows through CH_2O (e.g., NMHC, and branches from CH_3OOH and acetone). The constraint of CH_2O to observations in these model simulations, rather than allowing the model to predict concentrations of CH_2O, limits the ability to segregate HO_x sources from CH_2O into the individual initiating species. Figure 7 shows median profiles of the following instantaneous HO_x sources calculated from observations: the primary source stemming from O_3 photolysis, the radical channel of CH_2O photolysis, the branch of CH_3OOH photolysis that does not flow through CH_2O (i.e., that which is not already included implicitly in the calculated source from constrained CH_2O), and the photolysis of H_2O_2 and HO_2NO_2. The source from ketones and ozoneolysis of alkenes are minor contributors and are not shown.

The total HO_x source during ARCTAS-B is nearly an order of magnitude larger than during ARCTAS-A in the boundary layer, and is larger by a factor of 4 in the free troposphere. Dry conditions and low J-O^1D photolysis rates during spring result in a suppressed primary source for HO_x from $O(^1D) + H_2O$ in the free troposphere, amplifying the importance of the reservoir sources. The flow through CH_2O is the second largest HO_x source in the free and upper troposphere, at about 25 % of the total during both seasons. The source from H_2O_2 is the largest component of the HO_x source in the middle and upper troposphere, at 45 % during spring and 30 % during summer. This emphasizes the importance of differences in H_2O_2 measurements during ARCTAS-A and TOPSE, as it has potential consequences for the total HO_x source.

4.2 Model versus observations of HO_x

Observations of OH and HO_2 are shown by the bar plots in Fig. 8a,b. During ARCTAS-A, concentrations of OH are markedly low. Twenty percent of all OH observations are at LOD (≤ 0.01 pptv), and nearly 40 % of the OH measurements below 2 km are at LOD. OH concentrations generally increase with altitude. During ARCTAS-B, OH maximizes in the middle troposphere at concentrations more than 4 times larger than those during spring. While springtime values of HO_2 are uniformly low with no vertical gradient (median values are 4 pptv or less), summertime values are largest near the surface (16.7 pptv) and decrease to 7–8 pptv above 8 km.

Model predictions of OH and HO_2 from the fully constrained model are shown by the bars in Fig. 8c,d. The thin solid lines in the figures reproduce the median observed profiles shown in the upper panels for direct comparison. Both the median concentrations and altitude gradient of OH are well represented by the box model during ARCTAS-A, with a median R-Obs/Calc (OH) of 0.96. Alternately, predictions of OH during ARCTAS-B show a gradual increase with altitude, and are generally biased lower than observations. Predictions of HO_2 are significantly and consistently larger than observations throughout the full middle and upper troposphere during both phases. The overestimate of HO_2 persists down to the surface during ARCTAS-A.

Tables 5 and 6 quantify statistical quantities (median R-Obs/Calc and r^2), calculated using the full set of model/measurement pairs within various altitude bins. The number of OH observations at LOD during ARCTAS-A (often reported as negative values) makes interpretation of R-Obs/Calc problematic. In the cases where both the OH measurement and the model calculation are less than the instrument LOD of 0.01 pptv the two values are assumed to agree and a value of "1" is assigned for R-Obs/Calc. The correlation between measurements and model predictions (r^2) decreases for OH at low altitudes, particularly during ARCTAS-A. While there is an offset between model predictions and observations of HO_2 throughout most of the domain, the correlation between the two is uniformly high during both phases.

4.2.1 OH during ARCTAS-A

To better quantify the amount of scatter in the OH observations during ARCTAS-A, Fig. 9 shows the OH observations plotted as a function of sorted (increasing) model predictions. Sorted model values are shown with black points. All data values (blue points) are retained as reported, including those below LOD. A running median of the observations along this sorted series is calculated using a bin size of 50 and is shown with the green line. There is no bias between this running median of observations and the sorted model values at low concentrations. Below an arbitrary threshold value of 0.04 ppt (vertical line in Fig. 9), the median R-Obs/Calc is 0.98, while the model over predicts OH at higher concentrations (median R-Obs/Calc of 0.86).

The scatter of observations around the model predictions is large compared to the instrument LOD. For the subset of data below the selected threshold, 98 % (2σ) of the observations are contained within ±0.05 pptv around model predictions (68 % or 1σ are within ±0.022 pptv). Because the scatter is symmetric around the model predictions, it is unlikely that a single missing process in the model, such as missing measurements of BrO, can explain the scatter. The 2σ total uncertainties in model predictions of OH are of similar magnitude, ranging from 0.03 to 0.05 pptv (see Appendix A and

Table A2). These levels of observational scatter and model uncertainty are at the order of magnitude of the ambient observations. Below 2 km, for example, more than 85 % of the OH observations are less than 0.05 pptv, and nearly 60 % are less than 0.022 pptv. This suggests that at lower altitudes during ARCTAS-A, the practicality of observationally-based analysis using OH data is limited.

4.2.2 OH during ARCTAS-B

During ARCTAS-B, the model persistently under predicts OH for all but the highest altitudes (see Fig. 8c), with an overall R-Obs/Calc of 1.25. The scatter of observations around sorted model concentrations for ARCTAS-B is shown in Fig. 10. In contrast to ARCTAS-A, there is a clear bias toward model under prediction at the lower concentrations (retaining the threshold of 0.04 pptv identified in Sect. 4.3.1), with a median R-Obs/Calc of 2.5. This model under prediction holds throughout most of the range of model predictions, with a switch to over predictions evident only at the highest concentrations. Recent studies have suggested that at high solar zenith angles, an additional source of OH from the reaction of electronically exited NO_2 with H_2O may result in a source of OH and HONO that rivals the magnitude of the primary source from $O(^1D) + H_2O$ (Li et al., 2008). However, including this source in the box model made negligible difference in radical production for ARCTAS-B conditions.

The source of OH is strongly impacted by the recycling of HO_2, which is significantly over predicted at higher altitudes and slightly under predicted at the surface during ARCTAS-B (Fig. 8d). To minimize the impact of imperfect predictions of HO_2 on predictions of OH, it is useful to examine the predicted and observed HO_2/OH ratios. Figure 11a shows that there is a clear tendency of the model to overestimate HO_2/OH at low NO. Further, discussion in Appendix A and Fig. A2 shows that the uncertainty in the NO measurement dominates the uncertainty in model predictions of OH, and that the uncertainty increases with lower NO concentrations. A sensitivity simulation is run whereby NO is universally increased by 16 pptv (the 2σ uncertainty of the NO measurement at concentrations less than 100 pptv). For this test simulation, the overall median R-Obs/Calc for OH decreases from 1.25 to 0.9 with a dependence on NO concentration. Figure 11b shows the resulting R-Obs/Calc (HO_2/OH). There is currently no reason to suspect a bias in the measurement of NO during ARCTAS-B. However, given the high sensitivity of OH predictions to changes of NO within the bounds of the uncertainty of the measurement, it is difficult to more rigorously diagnose the cause of the persistent under prediction of OH during ARCTAS-B.

4.2.3 Impact of BrO on HO_x during Arctic spring

Halogen chemistry can potentially impact HO_x by altering (decreasing) the HO_2/OH ratio, and also by increasing the total source of HO_x. BrO is formed during the bromine-driven catalytic destruction of O_3 which has been observed over the Arctic (Oltmans and Komhyr, 1986; Barrie et al., 1988). BrO converts HO_2 (and other organic peroxy radicals) to OH via production of HOBr followed by its photolysis (reactions from Table 1):

$$\mathrm{BrO + HO_2 \rightarrow HOBr + O_2} \qquad \text{(R10)}$$

$$\mathrm{BrO + CH_3O_2 \rightarrow 0.25(CH_2O + HO_2 + O_3) + 0.75(HOBr + CH_2O_2)} \qquad \text{(R11)}$$

$$\mathrm{HOBr} + h\nu \rightarrow \mathrm{Br + OH} \qquad \text{(R20)}$$

In addition to this halogen impact of decreasing the HO_2/OH ratio, the reaction of Br with CH_2O and other aldehydes can serve as a source of HO_x, e.g.,

$$\mathrm{Br + CH_2O \rightarrow HBr + CO + HO_2} \qquad \text{(R2)}$$

For most of the ARCTAS data, the source of HO_x from Reaction (R2) contributes less than 10 % to the total HO_x source. However, under conditions where the primary source of HO_x is sufficiently inhibited due to depleted O_3, this bromine-initiated HO_x source can become significant in the relative sense. Additionally, in the presence of high NO (> several hundred pptv) elevated concentrations of the bromine radical (Br) are produced by Reaction (R12) such that the HO_2 source from Reaction (R2) can exceed other photochemical HO_x sources:

$$BrO + NO \rightarrow Br + NO_2 \tag{R12}$$

One of the goals of ARCTAS was to identify observational evidence of these halogen driven impacts on hydrogen radical chemistry. Of the modeled ARCTAS-A data considered in this study, two flights included BrO measurements (423 modeled points), using a CIMS instrument (Neumann et al., 2010). BrO measurements ranged from values of up to 8 pptv at the surface to ∼1 pptv in the free troposphere (left panel of Fig. 12a). The right panel in Fig. 12a shows coincident measurements of O_3, and verifies that the aircraft sampling captured some incidences of depleted boundary layer O_3 likely associated with BrO. While the data are influenced by time of day and varying NO_x levels, there is some indication of a general decrease of surface level O_3 with increasing BrO for measurements below 200 m (Fig. 12b).

In its standard configuration, the LaRC steady state model is constrained to measurements of BrO when measurements are available; this approach assumes equilibrium between the active bromine gas-phase species based on the instantaneous value for BrO. Therefore the availability of this measurement allows an estimation of the instantaneous impact of bromine radicals on gas-phase chemistry without the requirement of including details of aqueous-phase processing and bromine activation in the model (e.g., see Liao et al., 2011). Model results including and then neglecting the measurements of BrO are compared to predict the instantaneous impact of bromine on the HO_x budget and cycling in this high latitude environment.

Points with $NO > 200$ pptv or with O_3 undergoing depletion events (< 15 ppbv) are identified as events that may experience a substantial relative increase in HO_x source due to reaction of Br with aldehydes, e.g., Reaction (R2). The remaining background points encompass more than 85 % of the data. The median relative increase in predicted OH for these background points due to bromine chemistry is 21 % (a 39 % increase for points below 2 km and a 12 % increase in the middle troposphere). However, this translates into very modest absolute concentration increases of < 0.01 pptv (maximum increase is 0.03 pptv). As described in Sect. 4.3.1, available measurements of OH are not sufficient to verify this small impact on OH. The accompanying predicted decrease in background HO_2 due to the halogen chemistry impact on HO_2/OH described above is ~4 % (0.22 pptv). This value is significantly less than the total difference between observations and predictions; e.g., for this subset of points, the median R-Obs/Calc (HO_2) improves from 1.69 to 1.61 when BrO is included in the model calculations. For comparison, Liao et al. (2011) predicted 10–12 % increases in OH due to bromine chemistry over Summit, Greenland during the spring 2007 $GSHO_x$ (Greenland Summit Halogen-HO_x) campaign and 8–10 % decreases in $HO_2 + RO_2$.

For the 15 points identified as likely HO_x source events due to pollution ($NO > 200$ pptv), the total HO_x source increases by a factor of 5, resulting in increases of OH and HO_2 on the order of 0.03 pptv and 0.4 pptv, respectively. For the points with depleted O_3 (42 points), the total HO_x source increases by 68 % as a result of bromine chemistry, resulting in an OH increase of 0.01 ppt and a HO_2 increase of 0.36 pptv.

Figure 13 is a case study time series of data from 16 April during a very low altitude leg over Prudhoe Bay to illustrate the various impacts of bromine chemistry on the predictions of HO_2 for different chemical environments. Altitude is shown in Fig. 13a, with observations of NO, BrO and O_3 in Fig. 13b–d. The ATHOS measurements of HO_2 for this flight leg are shown in Fig. 13e (black), along with model predictions of HO_2 without bromine chemistry (blue) and with bromine chemistry included (red). Potential HO_x source events are shown at UTC 3.910 (depleted O_3) and in the vicinity of 3.912 (elevated NO). In each case, the prediction of HO_2 is larger when bromine chemistry is included as a result of an increase in the total HO_x source. The agreement with measurements worsens in the O_3 depletion case, but improves to excellent agreement in the high NO case. Background conditions are shown in the vicinity 3.914, where NO drops to less than 10 pptv, and O_3 remains at concentrations > 20 ppbv In this case, predicted HO_2 decreases with the addition of bromine chemistry as a result of the halogen driven decrease of the HO_2/OH ratio, improving the agreement between model and observed HO_2.

4.2.4 HO_2

A systematic model over prediction of HO_2 was shown in Fig. 8 and Tables 5 and 6. Figure 14a shows that the R-Obs/Calc (HO_2) is correlated with temperature not only through the two high latitude ARCTAS phases, but also through the portions of the ARCTAS-CARB phase that reached low temperatures (shown in green). The absolute difference between observations and predictions of HO_2 for all three phases are shown in Fig. 14b. For temperatures below 260 K, there is a persistent bias of about 2.5 pptv during ARCTAS-A, and of 5 pptv during ARCTAS-B and ARCTAS-CARB. Stratospheric points for all three phases are shown in the figures with the black plus symbols. There does not appear to be any marked difference in the observation to model comparison for the stratospheric points relative to the tropospheric points.

Similar to these box model results, Mao et al. (2010) found an over prediction of HO_2 when comparing results from the chemical transport model GEOS-Chem to ATHOS measurements during ARCTAS-A, and speculated that a temperature-dependent aerosol loss of HO_2 could provide a sufficient additional sink to reconcile HO_2 measurements and theory. The loss of HO_2 to aerosol was proposed to proceed as a pseudo first-order loss rate, dependent upon the surface area of the aerosol and a reaction probability that is highly sensitive to temperature and based largely on Thornton et al. (2008). Additionally, Mao et al. (2010) proposed a novel aqueous phase chemistry process that bypasses the formation of H_2O_2, thus rendering the aerosol reaction a terminal loss of HO_y.

The results from Mao et al. (2010) are based on three-dimensional model predictions of physical parameters and chemical precursor fields, and are useful for assessing relative influences on the chemical system as a whole. However, to determine whether such a terminal loss of HO_2 to aerosol is sufficient to reconcile in-situ observations of HO_x with simultaneous observations of its precursors, the use of the observationally constrained box model provides a method of direct assessment. Direct measurements of HO_x, its precursors, and species and parameters impacting its loss (i.e., aerosol surface area and temperature) are used here to examine the proposed temperature-dependent heterogeneous loss of HO_2. The loss rate is calculated using an aerosol surface area density (SAD) and a reaction probability (γ):

$$HO_2 \text{ loss rate } = \frac{\text{SAD}}{\left\{\frac{4}{\gamma \varpi} + \frac{r_p}{D_g}\right\}} \tag{1}$$

where ϖ is the temperature-dependent mean molecular speed of HO_2, r_p is the particle radius, and D_g is the diffusion coefficient for HO_2. Unfortunately, measurements of aerosol SAD from the DC-8 are not available for altitudes above about 3 km during ARCTAS because the Ultra High Sensitivity Aerosol Spectrometer instrument was not functional above this altitude. Measurements of aerosol scattering@550 nm were available on the DC-8, however, and are used here as a proxy to estimate aerosol SAD. The relationship between SAD and aerosol scattering@550 nm can be obtained for altitudes up to 8 km during ARCTAS using measurements from the suite of instruments on board the P3-B aircraft (operated by the Hawaii Group for Environmental Aerosol Research; Clark, 1991); this relationship is then applied to observations of aerosol scattering@550 nm obtained from the DC-8 to obtain estimates of SAD values consistent with the DC-8 data set.

The aerosol SAD measurements from the P3-B are shown in Fig. 15a,b in blue. Below 4 km, local fire emissions result in very high aerosol SAD values (off scale in Fig. 15b) but as will be shown, a heterogeneous loss to aerosol at the lower altitudes has little impact on HO_2 due to the magnitude of competing gas phase losses of HO_x at these altitudes. Note that these values for aerosol SAD assume dry particles, and therefore have an uncertainty associated with them in the presence of sufficient relative humidity (RH). For these P3-B data, 3/4 of the points above 6 km are at less than 56 % RH. For these dry conditions, the uncertainty in SAD is likely less than about a factor of 2. Figure 15c,d shows the linear fits obtained using the correlation for SAD values

$< 30\,cm^2\,cm^{-3}$ and aerosol scattering@550 nm using measurements from the P3-B. Resulting estimates for SAD for the DC-8 using that linear fit applied to DC-8 measurements of aerosol scattering@550 are indicated with the white bars in Fig. 15a,b. Aerosol SAD estimates for the DC-8 are similar to those from the P3-B in both median and range. For comparison, the predicted aerosol SAD from the GEOS-Chem global model for the same subset of DC-8 points is also shown in the figure (gray bars), with median values up to a factor of ~2 larger than those from the airborne measurements. Given the uncertainty related to RH, the difference between the estimates from in-situ data and those from GEOS-Chem can be interpreted as a reasonable range of values for SAD in the high latitude upper troposphere.

To estimate values for the reaction probability (γ) for the HO_2 aerosol loss in Eq. (1), a temperature-dependent estimate is based on that described in Thornton et al. (2008), assuming a pH of 5 and a particle radius of 0.2 µm. The calculated reaction probability ranges from 0.06 near the surface to 0.7 in the upper troposphere. The assumption of a particle radius $(r_p) = 0.2\,\mu m$ in Eq. (1) will overestimate the loss rate when larger particles dominate; P3-B size distribution data suggest that above 6 km, ~60 % of the integrated surface area is from particles < 0.2 µm radius, on average. This in-situ based estimate of the terminal aerosol loss for HO_2 is shown in Fig. 16a,b (white bars) along with the corresponding loss calculated by GEOS-Chem along the DC-8 flight tracks (gray bars). The GEOS-Chem calculation employs a similar approach to that used here, but integrates throughout the full spectrum of the model-generated particle size distribution information. The two estimates for the HO_2 loss rate to aerosol are generally consistent, with that predicted by GEOS-Chem somewhat larger, particularly during summer, driven by the larger SAD in GEOS-Chem. For the fully constrained box model test used here, this aerosol loss for HO_2 will only be effective at decreasing concentrations of HO_2 if the magnitude of the estimated loss rate is competitive with the gas phase losses of HO_x, shown by the open triangles in Fig. 16a,b (including the HO_2 self reaction, reaction of HO_2 with RO_2 to form organic peroxides, and reaction of OH with NO_2 to form HNO_3). For altitudes near the surface, the gas phase losses clearly dominate the estimates for aerosol loss. In the upper troposphere, the aerosol loss approaches values of the gas-phase loss during ARCTAS-A, and reaches 20 to 30 % of the gas-phase loss during ARCTAS-B.

To test the impact of including this HO_2 loss to aerosol using the observationally constrained box model, the larger loss rates from GEOS-Chem are adopted to give an upper bound estimate of the HO_2 loss. The loss rate is assumed to be terminal, as in Mao et al. (2010). The resulting changes in the R-Obs/Calc HO_2 ratio are shown in Fig. 16c,d, where the blue (ARCTAS-A) and red (ARCTAS-B) bars show the standard model results, and the gray bars show results the HO_2 loss to aerosol adopted from GEOS-Chem is included. In the upper troposphere for ARCTAS-A, the predicted HO_2 concentration decreases by ~23 % as a result of the loss to aerosol. The impact during ARCTAS-B is more subdued as expected, due to the relatively larger competing gas-phase HO_x losses. In both phases, however, while this terminal loss of HO_2 to aerosol is shown to impact predictions of HO_2 concentrations, it is clearly not sufficient to reconcile HO_2 measurements and predictions during ARCTAS. A significant bias toward over prediction remains, particularly at upper altitudes, with the median R-Obs/Calc (HO_2) above 4 km equal to 0.66 during ARCTAS-A and equal to 0.72 during ARCTAS-B. The HO_2 loss to aerosol in the upper troposphere would need to be three times larger than those adopted from GEOS-Chem during ARCTAS-A and six times larger during ARCTAS-B in order to predict HO_2 at the approximate magnitude of observations. Because the reaction probabilities at the high altitude colder temperatures are already large, this would suggest that the increases would need to come largely from higher values of aerosol SAD. Because GEOS-Chem values of SAD used in the calculation of the loss rate are approximately twice as large as the dry-particle in-situ derivations, this would in turn imply that values of SAD would be required to be 6 to12 times larger than the in-situ-based estimate. Increases of this order of magnitude are generally outside of the range of uncertainty associated with measurements for this region.

4.2.5 Coupling HO_x and HO_x precursors

Figures 17 and 18 show predictions of HO_2, OH, CH_2O and H_2O_2 from a suite of model simulations. The standard fully constrained model simulation (heavy solid line), and that including the loss of HO_2 to aerosol (heavy dash-dot line) have been discussed previously. The figures also show several additional partially unconstrained simulations that test the ability of model photochemistry to sustain observed values of HO_x reservoir precursors (peroxides and CH_2O) by predicting one or more of those species from model photochemistry rather than constraining to observations. Predictions of peroxides are highly sensitive to the model assumptions for rainout and deposition loss; within the lowest km the H_2O_2 lifetime due to surface deposition dominates its near-surface total loss rate, and up to 4 km the assumed rainout lifetime is approximately equal to the photochemical lifetime for H_2O_2. Because the history of physical loss due to rainout and/or deposition for any given air mass is highly uncertain, additional model simulations are performed that neglect surface deposition and rainout loss (dry simulations) in order to provide a range of predictions that bracket likely scenarios for these losses. The figures also show median observed values from ARCTAS with $\pm 2\sigma$ instrument uncertainties (asterisks and horizontal lines), and median observations from TOPSE-sp are shown with the open triangles in Fig. 17 for comparison to ARCTAS-A.

The collective group of model predictions shows a persistent over prediction of HO_2 during both seasons. For both ARCTAS-A and -B, the prediction of HO_2 that is most consistent with observations comes from a dual unconstrained model simulation (thin black line), in which both peroxides and CH_2O are predicted from steady state. Above the boundary layer, predictions of HO_2 from this simulation are 30–40 % lower than those from the standard fully constrained run during ARCTAS-A, and they are 10–25 % lower during ARCTAS-B. However, the predictions of H_2O_2 and CH_2O from this simulation (thin black lines in Figs. 17c,d and 18c,d) are well below ARCTAS observations, emphasizing the inconsistency between measurements of HO_x and of its precursors during ARCTAS. The predictions of H_2O_2 during ARCTAS-A are of similar magnitude to those measured during TOPSE-sp, and it can be argued that both lie just within the range of ARCTAS H_2O_2 instrument 2σ uncertainty. Whether differences are within or outside of the range of measurement uncertainty, however, it is clear that these differences in predicted and measured HO_x precursor concentrations have important implications for the HO_x budget.

As discussed previously, predictions of OH during ARCTAS-A are consistent with observations in the median, but there is a clear under prediction of OH during ARCTAS-B for all but the highest altitudes (Figs. 17b and 18b). The blue thin dotted line in Fig. 18b shows OH predictions for ARCTAS-B from the sensitivity run using the fully constrained standard model where NO was universally increased by its 2σ uncertainty of 16 pptv (discussed in Sect. 4.3.2). This sensitivity run reproduces median observed OH concentrations in the middle and lower troposphere, while changes to HO_2 are minor (less than a few percent). This emphasizes the sensitivity of OH predictions to uncertainties in the NO measurement during ARCTAS.

Simulations were also run whereby the constraint of a single HO_x precursor is individually relaxed; i.e., peroxides are constrained to observations while CH_2O is predicted (green lines, see Figs. 17d and 18d) and CH_2O is constrained to observations while peroxides are predicted (purple lines, see Figs. 17c and 18c). The corresponding dashed green and purple lines show results from the dry simulations, whereby the rainout loss for the predicted precursor is neglected. In general, the impact on CH_2O predictions due to peroxide constraint is small. Predictions increase and are closer to observations above 8 km during ARCTAS-A and below 4 km during ARCTAS-B, however CH_2O predictions remain significantly lower than observations throughout most of the free troposphere during both phases, part (Figs. 17d and 18d). Alternately, when CH_2O is held constrained to observed values, the predicted H_2O_2 from the rainout and the dry simulations bracket observations for all but the very highest altitudes ($>$ 8 km) during both phases. Thus, while the model is unable to reproduce any consistency between observed concentrations of HO_x and of its precursors, it is possible to argue there is some consistency between measurements of CH_2O and H_2O_2 when CH_2O is forced to observations.

Observed levels of CH_2O cannot be explained by model photochemical theory, and the diurnally averaged lifetime of CH_2O is short enough to preclude a significant source from middle latitude transport (6–10 h during ARCTAS-A and 3–10 h during ARCTAS-B). Sources that are not included in the box model such as emission from the snowpack and/or direct emission from fires may explain a portion of the model under predictions at the lowest altitudes, but these surface sources are unlikely to have a persistent impact throughout the extent of the troposphere during ARCTAS-A. The instances of convection observed during ARCTAS-B are a likely mechanism for transport of surface levels of CH_2O into the upper troposphere. In addition, convective transport of very short lived precursors such as isoprene can have an impact on upper tropospheric CH_2O concentrations that persist beyond the observable levels of the precursors; however the model under predictions of CH_2O are persistent and not limited to convective events. Fried et al. (2003) suggested that a temperature-dependent branching of $CH_3O_2 + HO_2$ to directly produce CH_2O may be important in cold temperatures (Elrod et al., 2001); however including this branch in the model chemistry did not substantially change predicted concentrations of CH_2O.

Figure 19 shows that model predictions of acetaldehyde (CH_3CHO) during ARCTAS are lower than both of two independent measurements using the PTRMS and TOGA instruments. To investigate the magnitude of an additional photochemical source of CH_2O from oxidation of observed levels of acetaldehyde, the model is run in a mode to predict CH_2O while retaining all other constraints with the additional constraint of acetaldehyde. The higher values of CH_3CHO from PTRMS are used to give upper bound estimates. Predicted CH_2O increases by less than 3 pptv during ARCTAS-A, except for altitudes > 8 km, where predicted CH_2O increases by 7.5 pptv to explain approximately half of the discrepancy between the model and observations. During ARCTAS-B, predicted CH_2O increases by 20 pptv for altitudes above 2 km, explaining between 25–60 % of the discrepancy.

The estimate of an additional flux of CH_3CHO required to reproduce the larger observations measured by PTRMS ranges from 35–90 pptv day^{-1} during ARCTAS-A, and up to several hundred pptv day^{-1} during ARCTAS-B. While the lifetime of acetaldehyde is longer than that of formaldehyde (1–3 days during spring and ~1 day during summer), it is not long enough to support a sustained significant transport flux of this magnitude. Kwan et al. (2006) speculate that oxidation of organic aerosols could be a source of oxygenated volatile organic compounds (OVOCs), and propose that up to 70 pptv C day^{-1} (equivalent to 35 pptv day^{-1} CH_3CHO) is possible in the upper troposphere over North America. Another possible source of acetaldehyde might be due to oxidation of unmeasured higher hydrocarbons. The origin of such a source that is pervasive throughout the high latitude troposphere is unknown.

5 O_3 budget

The diurnally averaged gross photochemical formation and destruction of O_3 during the two ARCTAS phases is shown in Fig. 20a,b by the bars on either side of the zero line. For ARCTAS-B, the results shown are limited to the "background" points, described in Sect. 3.2. The median net O_3 photochemical tendencies are shown by the blue (ARCTAS-A) and red (ARCTAS-B) lines. O_3 gross formation ranges from 0.4–0.8 ppbv day^{-1} during ARCTAS-A, with the upper value occurring at 1–4 km. This rate is in general agreement with the range of calculations for TOPSE (Cantrell et al., 2003a; Stroud et al., 2004). The net photochemical production of O_3 during spring is zero throughout most of the troposphere, with a small net positive production at highest altitudes of 0.2 ppbv day^{-1}. This supports the conclusions of TOPSE, that in order to support the springtime build up of O_3 at high latitudes, a combination of both transport of O_3 from middle latitudes and gross photochemical production is required. During summer (ARCTAS-B), the background data shows a gross production of O_3 in the boundary layer and at the highest altitudes 2–4 ppbv day^{-1}, with a net photochemical production of 1–2 ppbv day^{-1}. The middle troposphere is characterized by net photochemical destruction of about 1 ppbv day^{-1}.

Given the persistent model over prediction of HO_2, it is instructive to determine if and how much the O_3 formation and destruction rates during ARCTAS would vary if observed HO_2 were considered, rather than model-calculated values. Figure 20c,d shows the revised gross production and destruction rates, and the net production calculated using the observed HO_2 values. Throughout the free troposphere during both phases and extending to the surface during ARCTAS-A, gross production rates are 25–50 % lower when using observed HO_2 (see Table 7). Gross destruction is similarly reduced, so that differences in the net O_3 production rate are negligible.

6 Summary

Observations obtained during ARCTAS were analyzed using the observationally constrained NASA Langley Research Center photochemical box model in order to assess the tropospheric photochemical cycling occurring over high latitudes and its impact on the O_3 budget. At high latitudes and particularly during the spring, low radiation, cold temperatures, and dry conditions suppress photochemistry such that concentrations of many of the radicals and precursor species are very low. The resulting relative uncertainties in measurements and model predictions are sufficiently large so as to preclude a rigorous photochemical assessment.

While model predictions of OH during the spring (ARCTAS-A) are in general agreement with measurements (R-Obs/Calc = 0.96), observations of OH are frequently at LOD. The low concentrations in the boundary layer and lower troposphere are shown to have observational scatter and model prediction uncertainties that are at the order of magnitude of the ambient concentrations, limiting the usefulness of further observational analysis. Alternately, during summer (ARCTAS-B), concentrations of OH are four times larger than during spring, but predictions of OH are persistently lower than observations for all but the highest OH concentrations (R-Obs/Calc = 1.25). The R-Obs/Calc

HO_2/OH ratio shows a clear trend with NO with largest over-predictions at low NO concentrations. The uncertainty in model predictions of OH associated with uncertainties in observational constraints is dominated by the NO measurement uncertainty, and is largest at low values of NO. Predicted OH is consistent with measurements (within 10 %) if NO is increased uniformly within the bounds of its 2σ uncertainty, though there is no reason to suspect a bias in NO measurement at this time.

The largest sources of HO_2 in the middle and upper troposphere during ARCTAS are photolysis of H_2O_2 and CH_2O. Predictions of HO_2 are up to a factor of two larger than measurements when H_2O_2 and CH_2O are constrained to their observed values, highlighting the inconsistency between measurements of HO_2 and of its reservoir precursor species within the context of the box model mechanism. The temperature dependent terminal loss of HO_2 to aerosol proposed by Mao et al. (2010) decreased model predictions of HO_2 by ~23 % during ARCTAS-A, but was not sufficient to reconcile the differences between measured and predicted HO_2.

A comparison of measurements during ARCTAS-A and at high latitudes during the spring portion of the 2000 TOPSE field campaign revealed strikingly consistent measurements of temperature, water vapor, CO, NO, NMHCs, and CH_2O. However, differences were apparent in measurements of peroxides, with those during TOPSE several hundred pptv lower than during ARCTAS. A reverse bias is seen for CH_3OOH, with observations during ARCTAS-A 50–70 % lower than during TOPSE. The similarity in physical conditions and photochemical precursors precludes obvious differences in transport, rainout, or in the photochemical budget terms as a cause of the difference. The cause of this difference in peroxides remains unresolved and has important implications for the Arctic HO_x budget.

The box model photochemistry alone is unable to explain observed concentrations of CH_2O or H_2O_2 during ARCTAS; observations are larger than box model predictions by factors of ~2–3 during spring and by 50 %–200 % during summer. Predictions of HO_2 resulting from these combined lower model predicted precursor values are more consistent with observed HO_2, further highlighting the inconsistency between the measurements of HO_x and its precursors. Sensitivity simulations were also run where CH_2O was predicted while keeping peroxides constrained to observations, and vice versa, with peroxides were predicted while using constraint of observed CH_2O. Photochemistry resulting from observed concentrations of peroxides is unable to reproduce observed values of CH_2O. However, when the model is constrained to observed CH_2O, predictions of H_2O_2 using a range of rainout loss rates bracket observations.

Observations of acetaldehyde are larger than model predictions, and can provide an additional photochemical source of CH_2O that can explain up to half of the discrepancy between the model and measurements for portions of the troposphere. A source to explain larger acetaldehyde concentrations could be a result of oxidation of organic aerosols and/or unmeasured NMHC species, but the origin of such a precursor(s) that is pervasive throughout the higher latitudes is unknown.

Gross O_3 production during ARCTAS-A maximizes at 0.8 ppbv d^{-1} from 1–4 km, which is generally consistent with estimates from TOPSE. The net photochemical tendency is zero throughout the troposphere, indicating that transport of O_3 from middle latitudes is necessary to explain the springtime buildup of O_3 over high latitudes. During ARCTAS-B, there is a gross photochemical O_3 production of 2–4 ppbv d^{-1} in the boundary layer and at highest altitudes, with net photochemical tendencies of < 2 ppbv day^{-1}, while the middle troposphere is a net photochemical sink for O_3. The use of observed concentrations of HO_2 rather than model predictions decreased the gross photochemical formation rates above the boundary layer by 25–50 %. However, because the gross destruction of O_3 is reduced by a similar amount, the net photochemical production was relatively unaffected by the choice of modeled or measured HO_2.

Appendix A

Model uncertainty analysis

Sources of uncertainty in model predictions include uncertainties in kinetic and photolytic rate constants, and uncertainties in measurements of constraining observations. One method of estimating the model uncertainty uses a Monte Carlo approach, which can be executed for typical meteorological and chemical conditions for a region(s) of interest. Median observed values are found for lower (0–4 km), middle (4–8 km) and upper ($>$ 8 km) altitudes during each of the two ARCTAS phases. For each of these six sets of median conditions, the model uncertainty due to kinetics was calculated by running 2500 simulations whereby each of 105 model kinetic reaction rates and 16 photolytic rates was randomly and independently varied within its referenced 1σ uncertainty (Sander et al., 2006; Atkinson et al., 2005). The resulting range in predictions of radical species was used to find the model predictive uncertainty (converted to 2σ) due to kinetic uncertainties.

To evaluate uncertainty due to constraining species, another set of Monte Carlo simulations was performed for the six sets of median input conditions, whereby each of seven selected constraining species was randomly and independently varied within the 1σ measurement uncertainty for a 60 s average (Table A1). The resulting 2σ uncertainties in model predictions of OH, HO_2 are shown in Tables 6 and 7 for ARCTAS-A and ARCTAS-B. A total model uncertainty is estimated using a quadrature sum of these two components.

Because these uncertainty estimates are based on a limited set of input conditions, they should be interpreted as representative of a general bulk analysis of the data. Uncertainties for the individual data points will vary, depending upon the meteorology and chemical regime (i.e., dominant reactions). Rigorous calculation of uncertainties for each individual data point using the Monte Carlo approach would require an exorbitant amount of computing time. To estimate the predictive uncertainty for an individual data point, a “Sensitivity” approach may be employed, whereby each data point is run N times ($N = N_{con} + N_{kin}$), where N_{con} is the number of observational constraints selected to consider, and N_{kin} is the number of kinetic reactions selected to consider. For these sensitivity simulations, the component of interest (an observational constraint or a reaction rate) is increased by its 1σ uncertainty, and the absolute value of the relative difference in radical predictions is calculated. A quadrature sum of uncertainties obtained from each considered component gives an estimate of the total combined uncertainty for that individual data point. For comparison to the Monte Carlo results, Tables A2 and A3 also show the medians of the combined uncertainties obtained using the sensitivity approach for the 7 constraints listed in Table A1.

References

Apel, E.C, Hills A. J., Lueb, R., Zindel, S., Eisele, S., and Riemer, D. D.: A fast-GC/MS system to measure C_2 to C_4 carbonyls and methanol aboard aircraft, J. Geophys. Res., 108, 8794, doi:10.1029/2002JD003199, 2003.

Apel, E. C., Olson, J. R., Crawford, J. H., Hornbrook, R. S., Hills, A. J., Cantrell, C. A., Emmons, L. K., Knapp, D. J., Hall, S., Mauldin III, R. L., Weinheimer, A. J., Fried, A., Blake, D. R., Crounse, J. D., Clair, J. M. St., Wennberg, P. O., Diskin, G. S., Fuelberg, H. E., Wisthaler, A., Mikoviny, T., Brune, W., and Riemer, D. D.: Impact of the deep convection of isoprene and other reactive trace species on radicals and ozone in the upper troposphere, Atmos. Chem. Phys., 12, 1135–1150, doi:10.5194/acp-12-1135-2012, 2012.

Atkinson, R., Baulch, D. L., Cox, R. A., Crowley, J. N., Hampson, R. F., Hynes, R. G., Jenkin, M. E., Rossi, M. J., Troe, J., and IUPAC Subcommittee: Evaluated kinetic and photochemical data for atmospheric chemistry: Volume II – gas phase reactions of organic species, Atmos. Chem. Phys., 6, 3625–4055, doi:10.5194/acp-6-3625-2006, 2006.

Atlas, E. L., Ridley, B. A., and Cantrell, C. A.: The tropospheric ozone production about the Spring Equinox (TOPSE) Experiment: Introduction, J. Geophys. Res., 108, 8353, doi:10.1029/2002JD003172, 2003.

Barrie, L. A., Bottenhein, J. W., Schnell, R. C., Crutzen, P. J., and Rasmussen: R. A.: Ozone destruction and photochemical reactions at polar sunrise in the lower Arctic atmosphere, Nature, 334, 138–141, 1988.

Browne, E. C., Perring, A. E., Wooldridge, P. J., Apel, E., Hall, S. R., Huey, L. G., Mao, J., Spencer, K. M., Clair, J. M. St., Weinheimer, A. J., Wisthaler, A., and Cohen, R. C.: Global and regional effects of the photochemistry of $CH_3O_2NO_2$: evidence from ARCTAS, Atmos. Chem. Phys., 11, 4209–4219, doi:10.5194/acp-11-4209-2011, 2011.

Brune, W. H., Tan, D., Faloona, I. F., Jaeglé, L., Jacob, D. J., Heikes, B. G., Snow, J., Kondo, Y., Shetter, R., Sachse, G. W., Anderson, B., Gregory, G. L., Vay, S., Singh, H. B., Davis, D. D., Crawford, J. H., and Blake, D. R.: OH and HO_2 chemistry in the North Atlantic free Troposphere, Geophys. Res. Lett., 26, 3077–3080, 1999.

Cantrell, C. A., Mauldin, L., Zondlo, M., Eisele, F., Kosciuch, E., Shetter, R., Lefer, B., Hall, S., Campos, R., Ridley, B., Walega, J., Fried, A., Wert, B., Flocke, F., Weinheimer, A., Hannigan, J., Coffey, M., Atlas, E., Stephens, S., Heikes, B., Snow, J., Blake, D., Blake, N., Katzenstein, A., Lopez, J., Browell, E. V., Dibb, J., Scheuer, E., Seid, G., and Talbot, R.: Steady state free radical budgets and ozone photochemistry during TOPSE, J. Geophys. Res., 108, 8361, doi:10.1029/2002JD002198, 2003a.

Cantrell, C. A., Edwards, G. D., Stephens, S., Mauldin, R. L., Zondlo, M. A., Kosciuch, E., Eisele, F. L., Shetter, R. E., Lefer, B. L., Hall, S., Flocke, F., Weinheimer, A., Fried, A., Apel, E., Kondo, Y., Blake, D. R., Blake, N. J., Simpson, I. U. J., Bandy, A. R., Thornton, D. C., Heikes, B. G., Singh, H. B., Brune, W. H., Harder, H., Martinez, M., Jacob, D. J., Avery, M. A., Barrick, J. D., Sachse, G. W., Olson, J. R., Crawford, J. H., and Clarke, A. D.: Peroxy radical behavior during the Transport and Chemical Evolution over the Pacific (TRACE-P) campaign as measured aboard the NASA P-3B aircraft, J. Geophys. Res., 108, 8797, 2003b.

Chen, G., Davis, D., Crawford, J., Hutterli, L. M., Huey, L. G., Slusher, D., Mauldin, L., Eisele, F., Tanner, D., Dibb, J., Buhr, M., McConnell, J., Lefer, B., Shetter, R., Blake, D., Song, C. H., Lombardi, K., and Arnoldy, J.: A reassessment of HO_x South Pole chemistry based on observations recorded during ISCAT 2000, Atmos. Environ., 38, 5451–5461, 2004.

Clark, A. D.: A thermo-optic technique for in-situ analysis of size-resolved aerosol physicochemistry, Atmos. Environ. A, 25, 3–4, 635–644, 1991.

Comiso, J. C., Parkinson, C. L., Gersten, R., and Stock, L.: Accelerated decline in the Arctic sea ice cover, Geophys. Res. Lett., 35, L01703, doi:10.1029/2007GL031972, 2008.

Crawford, J., Davis, D., Olson, J., Chen, G., Liu, S., Gregory, G., Barrick, J., Sachse, G., Sandholm, S., Heikes, B., Singh, H., and Blake, D.: Assessment of upper tropospheric HO_x sources over the tropical Pacific based on NASA GTE/PEM data: Net effect on HO_x and other photochemical parameters, J. Geophys. Res., 104, 16255–16273, 1999.

Crounse, J. D., McKinney, K. A., Kwan, A. J., and Wennberg, P. O.: Measurement of gas-phase hydroperoxides by chemical ionization mass spectrometry, Anal. Chem., 78, 6726–6732, 2006.

Diskin, G. S.: Open-path airborne tunable diode laser hydrometer, diode lasers and applications in atmospheric sensing, edited by: Fried, A., SPIE Proc., 4817, 196–204, 2002.

Elrod, M. J., Ranschaert, D. L., and Schneider, N. L.: Direct kinetic study of the temperature dependence of the CH_2O branching channel for the $CH_3O_2 + HO_2$ reaction, Int. J. Chem. Kinet., 33, 363–376, 2001.

Emmons, L. K., Hess, P., Klonecki, A., Tie, X., Horowitz, L., Lamarque, J.-F., Kinnison, D., Brasseur, G., Atlas, E., Browell, E., Cantrell, C., Eisele, F., Mauldin, R. L., Merrill, J., Ridley, B., and Shetter, R.: Budget of tropospheric ozone during TOPSE from two Chemical transport models, J. Geophys. Res., 108, 8372, doi:10.1029/2002JD002665, 2003.

Evans, M. J., Jacob, D. J., Atlas, E., Cantrell, C. A., Eisele, F., Flocke, F., Fried, A., Mauldin, R. L., Ridley, B. A., Wert, B., Talbot, R., Blake, D., Heikes, B., Snow, J., Walega, J. Weinheimer, A. J., and Dibb, J.: Coupled evolution of BrO_x-ClO_x-HO_x-NO_x chemistry during bromine-catalyzed ozone depletion events in the arctic boundary layer, J. Geophys. Res., 108, 8368, doi:10.1029/2002JD002732, 2003.

Faloona, I., Tan, D., Lesher, R. L., Hazen, N. L., Frame, C. L., Simpas, J. B., Harder, H., Martinez, M., DiCarlo, P., Ren, X., and Brune, W. H.: A laser-induced fluorescence instrument for detecting tropospheric OH and HO_2: characteristics and calibration, J. Atmos. Chem., 47, 139–167, 2004.

Fisher, J. A., Jacob, D. J., Purdy, M. T., Kopacz, M., Le Sager, P., Carouge, C., Holmes, C. D., Yantosca, R. M., Batchelor, R. L., Strong, K., Diskin, G. S., Fuelberg, H. E., Holloway, J. S., Hyer, E. J., McMillan, W. W., Warner, J., Streets, D. G., Zhang, Q., Wang, Y., and Wu, S.: Source attribution and interannual variability of Arctic pollution in spring constrained by aircraft (ARCTAS, ARCPAC) and satellite (AIRS) observations of carbon monoxide, Atmos. Chem. Phys., 10, 977–996, doi:10.5194/acp-10-977-2010, 2010.

Frey, M. M., Hutterli, M. A., Chen, G., Sjostedt, S. J., Burkhart, J. F., Friel, D. K., and Bales, R. C.: Contrasting atmospheric boundary layer chemistry of methylhydroperoxide (CH_3OOH) and hydrogen peroxide (H_2O_2) above polar snow, Atmos. Chem. Phys., 9, 3261–3276, doi:10.5194/acp-9-3261-2009, 2009.

Fried, A., Wang, Y., Cantrell, C., Wert, B., Walega, J., Ridley, B., Atlas, E., Shetter, R., Lefer, B., Coffey, M. T., Hannigan, J., Blake, D., Blake, N., Meinardi, S., Talbot, B., Dibb, J., Scheuer, E., Wingenter, O., Snow, J., Heikes, B., and Ehhalt, D.: Tunable diode laser measurements of formaldehyde during the TOPSE 2000 study: distributions, trends, and model comparisons, J. Geophys. Res., 108, 8365, doi:10.1029/2002JD002208, 2003.

Fuelberg, H. E., Harrigan, D. L., and Sessions, W.: A meteorological overview of the ARCTAS 2008 mission, Atmos. Chem. Phys., 10, 817–842, doi:10.5194/acp-10-817-2010, 2010.

Jacob, D. J., Crawford, J. H., Maring, H., Clarke, A. D., Dibb, J. E., Emmons, L. K., Ferrare, R. A., Hostetler, C. A., Russell, P. B., Singh, H. B., Thompson, A. M., Shaw, G. E., McCauley, E., Pederson, J. R., and Fisher, J. A.: The Arctic Research of the Composition of the Troposphere from Aircraft and Satellites (ARCTAS) mission: design, execution, and first results, Atmos. Chem. Phys., 10, 5191–5212, doi:10.5194/acp-10-5191-2010, 2010.

Kwan, A. J., Crounse, J. D., Clarke, A., Shinozuka, Y., Anderson, B. E., Crawford, J. H., Avery, M. A., McNaughton, C., Brune, W. H., Singh, H. B., and Wennberg, P. O.: On the flux of oxygenated volatile organic compounds from organic aerosol oxidation, Geophys. Res. Lett., 33, L15815, doi:10.1029/2006GL026144, 2006.

Law, K. S. and Stohl, A.: Arctic air pollution: origins and impacts, Science, 315, 1537–1540, doi:10.1126/science.1137695, 2007.

Lee, M., O'Sullivan, D., Noone, K. B., and Heikes, B. G.: HPLC method for determination of H_2O_2, C_1 and C_2 hydroperoxides in the atmosphere, J. Atmos. Ocean. Tech., 12, 1060–1070, 1995.

Lemke, P., Ren, J., Alley, R. B., Allison, I., Carrasco, J., Flato, G., Fujii, Y., Kaser, G., Mote, P., Thomas, R. H., and Zhang, T.: Observations: Changes in Snow, Ice and Frozen Ground, Climate Change 2007: The Physical Science Basis. Contribution of Working Group I to the Fourth Assessment Report of the Intergovernmental Panel on Climate Change, edited by: Solomon, S., Qin, D., Manning, M., Chen, Z., Marquis, M., Averyt, K. B., Tignor, M., and Miller, H. L., Cambridge University Press, Cambridge, UK and New York, NY, USA, 2007.

Li, S., Matthews, J., and Sinha, A.: Atmospheric hydroxyl radical production from electronically excited NO_2 and H_2O, Science, 319, 1657–1660, 2008.

Liao, J., Huey, L. G., Tanner, D. J., Brough, N., Brooks, S., Dibb, J. E., Stutz, J., Thomas, J. L., Lefer, B., Haman, C., and Gorham, K.: Observations of hydroxyl and peroxy radicals and the impact of BrO at Summit, Greenland in 2007 and 2008, Atmos. Chem. Phys., 11, 8577–8591, doi:10.5194/acp-11-8577-2011, 2011.

Logan, J. A., Prather, M. J., Wofsy, S. C., and McElroy, M. B.: Tropospheric chemistry: a global perspective, J. Geophys. Res., 86, 7210–7254, 1981.

Lurmann, F. W., Lloyd, A. C., and Atkinson, R.: A chemical mechanism for use in long-range transport/acid deposition computer modeling, J. Geophys. Res., 91, 10905–10936, 1986.

Madronich, S. and Flocke, S.: The role of solar radiation in atmospheric chemistry, in: Handbook of Environmental Chemistry, edited by: Boule, P., Springer, New York, 1–26, 1998.

Mao, J., Jacob, D. J., Evans, M. J., Olson, J. R., Ren, X., Brune, W. H., Clair, J. M. St., Crounse, J. D., Spencer, K. M., Beaver, M. R., Wennberg, P. O., Cubison, M. J., Jimenez, J. L., Fried, A., Weibring, P., Walega, J. G., Hall, S. R., Weinheimer, A. J., Cohen, R. C., Chen, G., Crawford, J. H., McNaughton, C., Clarke, A. D., Jaeglé, L., Fisher, J. A., Yantosca, R. M., Le Sager, P., and Carouge, C.: Chemistry of hydrogen oxide radicals (HO_x) in the Arctic troposphere in spring, Atmos. Chem. Phys., 10, 5823–5838, doi:10.5194/acp-10-5823-2010, 2010.

Mauldin III, R. L., Tanner, D. J., and Eisele, F. L.: Measurements of OH during PEM-Tropics A, J. Geophys. Res., 104, 5817–5827, 1999.

Neuman, J. A., Nowak, J. B., Huey, L. G., Burkholder, J. B., Dibb, J. E., Holloway, J. S., Liao, J., Peischl, J., Roberts, J. M., Ryerson, T. B., Scheuer, E., Stark, H., Stickel, R. E., Tanner, D. J., and Weinheimer, A.: Bromine measurements in ozone depleted air over the Arctic Ocean, Atmos. Chem. Phys., 10, 6503–6514, doi:10.5194/acp-10-6503-2010, 2010.

Olson, J. R., Crawford, J. H., Chen, G., Brune, W. H., Faloona, I. C., Tan, D., Harder, H., and Martinez, M.: A reevaluation of airborne HO_x observations from NASA field campaigns, J. Geophys Res., 111, D10301, doi:10.1029/2005JD006617, 2006.

Oltmans, S. J.: Surface ozone measurements in clean air, J. Geophys. Res., 86, 1174–1180, 1981.

Oltmans, S. J. and Komhyr, W.: Surface ozone distributions and variations from 1973–1984: measurements at the NOAA geophysical monitoring for climatic change baseline observatories, J. Geophys. Res., 91, 5229–5236, doi:10.1029/JD091iD04p05229, 1986.

Orlando, J. J. and Tyndall, G. S.: Rate coefficients for the thermal decomposition of $BrONO_2$ and the heat of formation of $BrONO_2$, J. Phys. Chem., 100, 19298–19405, 1996.

Quinn, P. K., Bates, T. S., Baum, E., Doubleday, N., Fiore, A. M., Flanner, M., Fridlind, A., Garrett, T. J., Koch, D., Menon, S., Shindell, D., Stohl, A., and Warren, S. G.: Short-lived pollutants in the Arctic: their climate impact and possible mitigation strategies, Atmos. Chem. Phys., 8, 1723–1735, doi:10.5194/acp-8-1723-2008, 2008.

Ren, X., Mao, J., Brune, W. H., Cantrell, C. A., Mauldin III, R. L., Hornbrook, R. S., Kosciuch, E., Olson, J. R., Crawford, J. H., Chen, G., and Singh, H. B.: Airborne intercomparison of HO_x measurements using laser-induced fluorescence and chemical ionization mass spectrometry during ARCTAS, Atmos. Meas. Tech. Discuss., 5, 2529–2565, doi:10.5194/amtd-5-2529-2012, 2012.

Rinsland, C. P., Coheur, P. F., Herbin, H., Clerbaux, C., Boone, C., Bernath, P., and Chiou, L. S.: Detection of elevated tropospheric hydrogen peroxide (H_2O_2) mixing ratios in atmospheric chemistry experiment (ACE) subtropical infrared solar occultation spectra, J. Quant. Spectrosc. Ra., 107, 340–348, 2007.

Sachse, G., Hill, G., Wade, L., and Perry, M.: Fast-response, high-precision carbon monoxide sensor using a tunable diode laser absorption technique, J. Geophys. Res., 92, 2095–2081, 2008.

Sander, S. P., Fridl, R. R., Ravishankara, A. R., Golden, D. M., Kolb, C. E., Kurylo, M. J., Molina, M. J., Moortgat, G. K., Finlayson-Pitts, B. J., Wine, P. H., Huie, R. E., and Orkin, V. L.: Chemical kinetics and photochemical data for use in atmospheric studies, Evaluation Number 15, JPL Publ., 06-2, 2006.

Scheuer, E., Talbot, R. W., Dibb, J. E., Seid, G. K., de Bell, L., and Lefer, G.: Seasonal distributions of fine aerosol sulfate in the North American Arctic Basin during TOPSE, J. Geophys. Res., 108, 8370, doi:10.1029/2001JD001364, 2003.

Shaw, G. E.: The Arctic phase phenomenon, B. Am. Meterol. Soc., 76, 2403–2413, 1995.

Shetter, R. E. and Muller, M.: Photolysis frequency measurements using actinic flux spectroradiometry during the PEM-Tropics mission: Instrumentation description and some results, J. Geophys. Res., 104, 5647–5661, 1999.

Shindell, D. T., Faluvegi, G., Bauer, S. E., Koch, D. M., Unger, N., Menon, S., Miller, R. L., Schmidt, G. A., and Streets, D. G.: Climate response to projected changes in short-lived species under an A1B scenario from 200–2050 in the GISS climate model, J. Geophys Res., 112, D20103, doi:10.1029/2007D008753, 2007.

Shindell, D. T., Chin, M., Dentener, F., Doherty, R. M., Faluvegi, G., Fiore, A. M., Hess, P., Koch, D. M., MacKenzie, I. A., Sanderson, M. G., Schultz, M. G., Schulz, M., Stevenson, D. S., Teich, H., Textor, C., Wild, O., Bergmann, D. J., Bey, I., Bian, H., Cuvelier, C., Duncan, B. N., Folberth, G., Horowitz, L. W., Jonson, J., Kaminski, J. W., Marmer, E., Park, R., Pringle, K. J., Schroeder, S., Szopa, S., Takemura, T., Zeng, G., Keating, T. J., and Zuber, A.: A multi-model assessment of pollution transport to the Arctic, Atmos. Chem. Phys., 8, 5353–5372, doi:10.5194/acp-8-5353-2008, 2008.

Singh, H. B., Brune, W. H., Crawford, J. H., Jacob, D. J., and Russell, P. B.: Overview of the summer 2004 Intercontinental Chemical Transport Experiment – North America (INTEX-A), J. Geophys. Res., 111, D24S01, doi:10.1029/2006JD007905, 2006.

Singh, H. B., Anderson, B. E., Brune, W. H., Cai, C., Cohen, R. C., Crawford, J. H., Cubison, M. J., Czech, E. P., Emmons, L., Fuelberg, H. E., Huey, G., Jacob, D. J., Jimenez, J. L., Kaduwela, A., Kondo, Y., Mao, J., Olson, J. R., Sachse, G. W., Vay, S. A., Weinheimer, A., Wennberg, P. O., Wisthaler, A., and the ARCTAS Science Team: Pollution influences on atmospheric composition and chemistry at high northern latitudes: Boreal and California forest fire emissions, Atmos. Environ., 44, 4553–4564, doi:10.1016/jatmosenv.2010.08.026, 2010.

Slusher, D. L., Huey, L. G., Tanner, D. J., Flocke, F. M., and Roberts, J. M.: A thermal dissociation-chemical ionization mass spectrometry (TD-CIMS) technique for the simultaneous measurement of peroxyacyl nitrates and dinitrogen pentoxide, J. Geophys. Res., 109, D19315, doi:10.1029/2004JD004670, 2004.

Snow, J. A., Heikes, B. G., Merrill, J. T., Wimmers, A. J., Moody, J. L., and Cantrell, C. A.: Winter-spring evolution and variability of HO_x reservoir species, hydrogen peroxide, and methyl hydroperoxide in the northern middle to high latitudes, J. Geophys. Res., 108, 8362, doi:10.1029/2002JD002172, 2003.

Snow, J. A., Heikes, B. G., Shen, H., O'Sullivan, D. W., Fried, A., and Walega, J.: Hydrogen peroxide, methyl hydroperoxide, and formaldehyde over North America and the North Atlantic, J. Geophys. Res., 112, D12S07, doi:10.1029/2006JD007746, 2007.

Soller, R., Nicovich, J., and Wine, P.: Temperature-dependent rate coefficients for the reactions of $Br(^2P_{3/2})$, $Cl(^2P_{3/2})$, and $O(^3P)$ with $BrONO_2$, J. Phys. Chem. A., 105, 1416–1422, 2001.

Stohl, A.: Characteristics of atmospheric transport into the Arctic troposphere, J. Geophys. Res., 111, D11306, doi:10.1029/2005JD006888, 2006.

Stroud, C., Madronich, S., Atlas, E., Cantrell, C., Fried, A., Wert, B., Ridley, B., Eisele, F., Mauldin, L., Shetter, R., Lefer, B., Flocke, F., Weinheimer, A., Coffey, M., Heikes, B., Talbot, R., and Blake, C.: Photochemistry in the Arctic free troposphere: Ozone budget and its dependence on nitrogen oxides and the production rate of free radicals, J. Atmos. Chem., 47, 107–138, 2004.

Thornton, J. A., Jaeglé, L., and McNeill, V. F.: Assessing known pathways for HO_2 loss in aqueous atmospheric aerosols: Regional and global impacts on tropospheric oxidants, J. Geophys. Res., 113, D05303, doi:10.1029/2007jd009236, 2008.

von Glasow, R., von Kuhlmann, R., Lawrence, M. G., Platt, U., and Crutzen, P. J.: Impact of reactive bromine chemistry in the troposphere, Atmos. Chem. Phys., 4, 2481–2497, doi:10.5194/acp-4-2481-2004, 2004.

Weibring, P., Richter, D., Walega, J. G., and Fried, A.: First demonstration of a high performance difference frequency spectrometer on airborne platforms, Opt. Express., 15, 13476–13495, 2007.

Weinheimer, A. J., Walega, J. G., Ridley, B. A., Gary, G. L., Blake, D. R., Blake, N. J., Rowland, F. S., Sachse, G. W., Anderson, B. E., and Collins, J. E.: Meridional distributions of NO_x, NO_y and other species in the lower stratosphere and upper troposphere during AASE II, Geophys. Res. Lett., 21, 2583–2586, 1994.

Wisthaler, A., Hansel, A., Dickerson, R. R., and Crutzen, P. J.: Organic trace gas measurements by PTR-MS during INDOEX 1999, J. Geophys. Res., 107, 8024, doi:10.1029/2001JD000576, 2002.

Table 1. Bromine reactions included in the model.

Reaction	Rate	Reference	Reaction number
$Br + O_3 \rightarrow BrO + O_2$	$1.7 \times 10^{-11} e^{(-800/T)}$	Sander et al. (2006)	(R1)
$Br + CH_2O \rightarrow HBr + HO_2$	$7.7 \times 10^{-12} e^{(-580/T)}$	Atkinson et al. (2006)	(R2)
$Br + CH_3CHO \rightarrow HBr + MCO_3$	$1.8 \times 10^{-11} e^{(-460/T)}$	Atkinson et al. (2006)	(R3)
$Br + ALD_3 \rightarrow HBr + RCO_3$	$5.75 \times 10^{-11} e^{(-610/T)}$	Atkinson et al. (2006)	(R4)
$Br + HO_2 \rightarrow HBr + O_2$	$4.8 \times 10^{-12} e^{(-310/T)}$	Sander et al. (2006)	(R5)
$Br + BrONO_2 \rightarrow Br_2 + NO_3$	$1.78 \times 10^{-11} e^{(365/T)}$	NIST,Soller et al. (2001)	(R6)
$Br + C_2H_2 \rightarrow HBr + HO_2 + 2CO$	$6.35 \times 10^{-15} e^{(440/T)}$	Atkinson et al. (2006)	(R7)
$Br + C_2H_4 \rightarrow BrMCO_3$ + Products	$2.8 \times 10^{-13} e^{(224/T)} \cdot \left\{ \frac{B}{B + 8.5 \times 10^{12} e^{(-3200/T)}} \right\}$ where $B = 7.5 \times 10^{-12} [O_2]$	Atkinson et al. (2006)	(R8)
$HBr + OH \rightarrow Br + H_2O$	$5.5 \times 10^{-12} e^{(200/T)}$	Sander et al. (2006)	(R9)
$BrO + HO_2 \rightarrow HOBr + O_2$	$4.5 \times 10^{-12} e^{(460/T)}$	Sander et al. (2006)	(R10)
$BrO + CH_3O_2 \rightarrow 0.25(CH_2O + HO_2 + O_3) + 0.75(HOBr + CH_2O_2)$	5.7×10^{-12}	Atkinson et al. (2006)	(R11)
$BrO + NO \rightarrow Br + NO_2$	$8.8 \times 10^{-12} e^{(260/T)}$	Atkinson et al. (2006)	(R12)
$BrO + NO_2 + M \rightarrow BrONO_2$	Three-body rxn	Atkinson et al. (2006)	(R13)
$BrONO_2 + M \rightarrow BrO + NO$	$2.79 \times 10^{13} e^{(-12389/T)}$	Orlando and Tyndall (1996)	(R14)
$BrO + BrO \rightarrow 2Br + O_2$	2.7×10^{-12}	Atkinson et al. (2006)	(R15)
$BrO + BrO \rightarrow Br_2 + O2$	$2.9 \times 10^{-14} e^{(840/T)}$	Atkinson et al. (2006)	(R16)
$HBr \rightarrow$ rainout		Logan et al. (1981)	(R17)
$HOBr \rightarrow$ rainout		Logan et al. (1981)	(R18)
$BrONO_2 \rightarrow$ rainout		Logan et al. (1981)	(R19)
$HOBr + h\gamma \rightarrow Br + OH$		Sander et al. (2006)	(R20)
$BrONO_2 + h\gamma \rightarrow 0.15(Br + NO_3) + 0.85(BrO + NO_2)$		Sander et al. (2006)	(R21)
$Br_2 + h\gamma \rightarrow 2Br$		Sander et al. (2006)	(R22)
$BrO + h\gamma \rightarrow Br + O$		Sander et al. (2006)	(R23)

Table 2. Observations used for model constraints and/or predictive comparisons.

Species	Institution, Instrument*	Reference
Physical parameters (e.g., UTC, Latitude, Longitude, Pressure-Altitude, Temperature, Pressure)	NASA DFRC, REVEAL	
Overhead O_3 Column	NASA, OMI Satellite	http://toms.gsfc.nasa.gov/
Photolysis rates	NCAR, spectral radiometer	Shetter and Muller (1999)
Species for model constraint		
H_2O, CH_4, CO	NASA LaRC, TDLAS	Diskin et al. (2002) Sachse et al. (1987)
O_3, NO	NCAR, Chemiluminescence	Weinheimer et al. (1994)
NMHC	UCI, WAS-GC	Blake et al. (2003)
Acetone, methanol	U. Innsbrook, PTR-MS	Wisthaler et al. (2002)
MEK, ethanol	NCAR, GC-MS (TOGA)	Apel et al. (2003)
BrO, SO_2	Georgia Tech, CIMS	Slusher et al. (2004)
Optional constraints (can also be used for predictive comparisons):		
PAN	Georgia Tech, CIMS	Slusher et al. (2004)
HNO_3	UNH, mist chamber/IC	Scheuer et al. (2003)
CH_2O	NCAR, DFGAS	Webring et al. (2007)
Peroxides (H_2O_2, CH_3OOH)	Cal Tech, CIMS	Crounse et al. (2006)
Species for predictive comparisons		
OH, HO_2	Penn State, LIF (ATHOS)	Faloona et al. (2004)
OH, HO_2, HO_2+RO_2	NCAR, CIMS	Cantrell et al. (2003)

* REVEAL = Research Environment for Vehicle-Embedded Analysis on Linux, OMI = Ozone Monitoring Instrument, TDLAS=Tunable diode laser absorption spectroscopy, WAS-GC=Whole Air Sampling – Gas Chromatography, PTR-MS = Proton Transfer Reaction – Mass Spectrometry, GC-MS – Gas Chromatography – Mass Spectrometry, CIMS = Chemical Ionization Mass Spectrometry, IC= Ion Chromatography, LIF = Laser Induced Fluorescence.

Table 3. Median meteorological conditions.

Altitude	Temp (K)	H_2O (ppmv)	Inst. J-O^1D 10^{-5} s^{-1}	Inst. J-NO_2 10^{-2} s^{-1}
ARCTAS-A > 50° N				
> 8 km	224	80	1.04	1.39
6–8 km	229	148	0.68	1.17
4–6 km	242	296	0.84	1.17
2–4 km	251	614	0.46	0.95
0–2 km	257	1270	0.46	0.91
TOPSE-sp (Mar–Apr) > 50° N				
> 8 km	–	–	–	–
6–8 km	229	161	0.71	1.06
4–6 km	237	225	0.56	1.08
2–4 km	253	869	0.44	0.93
0–2 km	258	1368	0.32	0.79
ARCTAS-B > 50° N				
> 8 km	231	210	1.78	1.25
6–8 km	246	436	2.73	1.22
4–6 km	260	1783	2.14	1.06
2–4 km	273	6292	0.89	0.78
0–2 km	285	9967	1.05	0.51

Table 4. Diurnally averaged lifetimes (days) based on model calculations.

Altitude	CO	C_3H_8	C_2H_4	CH_2O	H_2O_2	CH_3OOH
			ARCTAS-A			
> 4 km	220	69	3.8	0.28	3.9	2.4
0–4 km	213	64	3.9	0.38	4.8	3.1
			ARCTAS-B			
> 4 km	69	18	1.3	0.16	1.8	1.0
0–4 km	63	14	1.4	0.32	3.0	1.3

Table 5. Median observed-to-calculated ratios and (r^2) for HO_x.

Altitude	ARCTAS-A OH (ATHOS) R-Obs/Calc (r^2)	HO_2 (ATHOS) R-Obs/Calc (r^2)
> 8 km	0.85 (0.64)	0.49 (0.74)
6–8 km	0.91 (0.64)	0.52 (0.85)
4–6 km	1.00 (0.71)	0.58 (0.86)
2–4 km	0.89 (0.38)	0.67 (0.84)
1–2 km	0.74 (0.04)	0.66 (0.58)
0–1 km	1.00 (0.18)	0.71 (0.67)

Table 6. Median observed-to-calculated ratios and (r^2) for HO_x.

Altitude	ARCTAS-B OH (ATHOS) R-Obs/Calc (r^2)	HO_2 (ATHOS) R-Obs/Calc (r^2)
> 8 km	0.88 (0.73)	0.60 (0.76)
6–8 km	1.27 (0.50)	0.61 (0.76)
4–6 km	1.45 (0.61)	0.73 (0.85)
2–4 km	1.32 (0.53)	0.86 (0.82)
1–2 km	1.48 (0.50)	1.10 (0.78)
0–1 km	1.46 (0.59)	1.28 (0.89)

Table 7. Changes in O_3 gross formation when using observed HO_2.

Altitude	ARCTAS-A Pct (ppbv day^{-1})	ARCTAS-B Pct (ppbv day^{-1})
> 8 km	−46 % (−0.20)	−34 % (−0.73)
6–8 km	−40 % (−0.14)	−28 % (−0.19)
4–6 km	−31 % (−0.15)	−24 % (−0.20)
2–4 km	−20 % (−0.16)	−10 % (−0.15)
1–2 km	−26 % (−0.20)	−0.6 % (−0.02)
0–1 km	−26 % (−0.12)	+7.6% (+0.28)

Table A1. 1σ uncertainties for selected input constraints on 60 s time average.

Constraint	1σ uncertainty for 60 s average	Reference
O_3	4.3 % (for $O_3 <= 10$ ppbv) 4 % (for $O_3 > 10$ ppbv)	A. Weinheimer, personal communication
CO	2 %	G. Diskin, personal communication
NO	8 pptv (for NO < 100 pptv) 10 pptv (for NO 100–1000 pptv) 60 pptv (for NO > 1000 pptv)	A. Weinheimer, personal communication
CH_3OOH	33 pptv + 27 % (for H_2O 0–230 ppmv) 33 pptv + (−6.07 + 13.87 log(H_2O)) % (for H_2O > 230 ppmv)	P. Wennberg, personal communication
H_2O_2	67 pptv + 27 % (ARCTAS-A) 67 pptv + 33 % (ARCTAS-B)	P. Wennberg, personal communication
H_2O	Greater of 5 % or 1 ppmv	G. Diskin, personal communication
CH_2O	$\sqrt{(12.2\,\%[CH_2O])^2 + (LOD_{(\sim 22\,ppt)})^2}$	A. Fried, personal communication

Table A2. 2σ uncertainty in model predictions for ARCTAS-A (fully constrained model).

	Sensitivity approach	Monte Carlo approach	Monte Carlo approach	Monte Carlo approach
Altitude	Median 2σ $HO_{2\,calc}$ Obs. Constraint (Relative)	2σ $HO_{2\,calc}$ Obs. Constraint Relative (pptv)	2σ $HO_{2\,calc}$ Kinetics Relative (pptv)	2σ $HO_{2\,calc}$ Combined Relative
> 8 km	0.24	0.25 (2.13)	0.29 (2.39)	0.38
4–8 km	0.22	0.21 (1.72)	0.26 (2.19)	0.33
0–4 km	0.20	0.14 (0.88)	0.24 (1.52)	0.28
Altitude	Median 2σ OH_{calc} Obs. Constraint (Relative)	2σ OH_{calc} Obs. Constraint Relative (pptv)	2σ OH_{calc} Kinetics Relative (pptv)	2σ OH_{calc} Combined Relative
> 8 km	0.60	0.56 (0.04)	0.41 (0.03)	0.69 (0.05)
4–8 km	0.64	0.58 (0.03)	0.36 (0.02)	0.68 (0.04)
0–4 km	0.68	0.50 (0.03)	0.31 (0.01)	0.59 (0.03)

Table A3. 2σ uncertainty in model predictions for ARCTAS-B (fully constrained model).

	Sensitivity approach	Monte Carlo approach	Monte Carlo approach	Monte Carlo approach
Altitude	Median 2σ $\mathrm{HO}_{2\,\mathrm{calc}}$ Obs. Constraint (Relative)	2σ $\mathrm{HO}_{2\,\mathrm{calc}}$ Obs. Constraint Relative (pptv)	2σ $\mathrm{HO}_{2\,\mathrm{calc}}$ Kinetics Relative (pptv)	2σ $\mathrm{HO}_{2\,\mathrm{calc}}$ Combined Relative
> 8 km	0.16	0.14 (2.60)	0.28 (5.01)	0.31
4–8 km	0.14	0.12 (2.22)	0.25 (4.56)	0.28
0–4 km	0.08	0.09 (1.52)	0.23 (4.02)	0.25
Altitude	Median 2σ $\mathrm{OH}_{\mathrm{calc}}$ Obs. Constraint (Relative)	2σ $\mathrm{OH}_{\mathrm{calc}}$ Obs. Constraint Relative (pptv)	2σ $\mathrm{OH}_{\mathrm{calc}}$ Kinetics Relative (pptv)	2σ $\mathrm{OH}_{\mathrm{calc}}$ Combined Relative
> 8 km	0.34	0.33 (0.08)	0.35 (0.08)	0.48
4–8 km	0.44	0.51 (0.08)	0.33 (0.05)	0.61
0–4 km	0.32	0.29 (0.02)	0.33 (0.03)	0.44

Title Page
Abstract | Introduction
Conclusions | References
Tables | Figures
◀| |▶
◀ ▶
Back | Close
Full Screen / Esc
Printer-friendly Version
Interactive Discussion

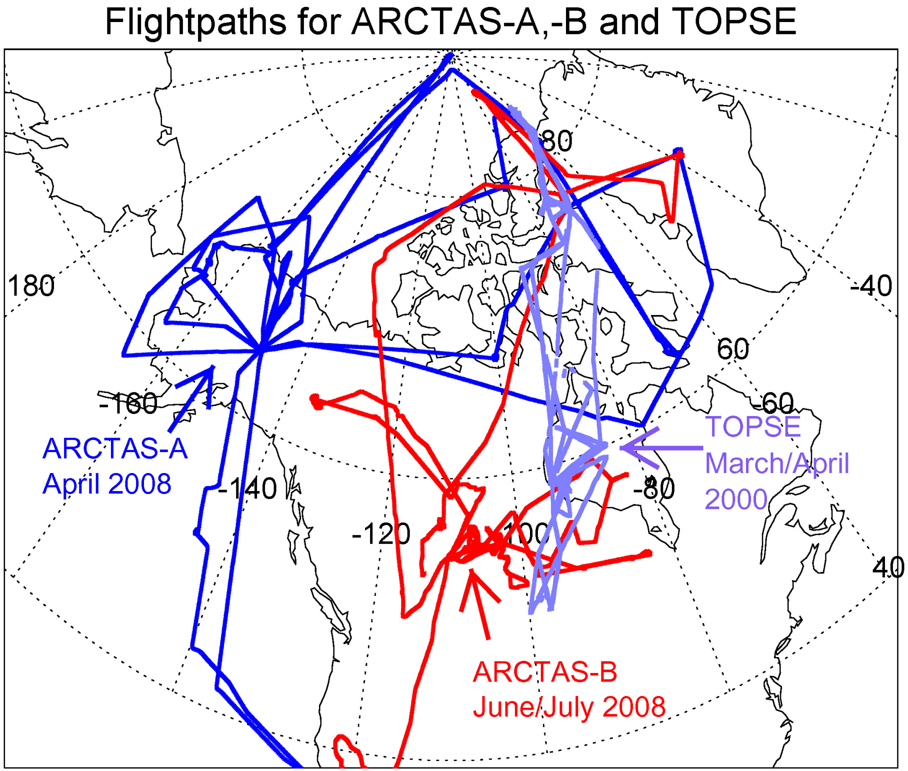

Fig. 1. Flight paths for the NASA DC-8 during ARCTAS-A and -B, and for the NCAR C-130 during TOPSE-sp (subset of TOPSE data obtained during March and April and north of 50° N).

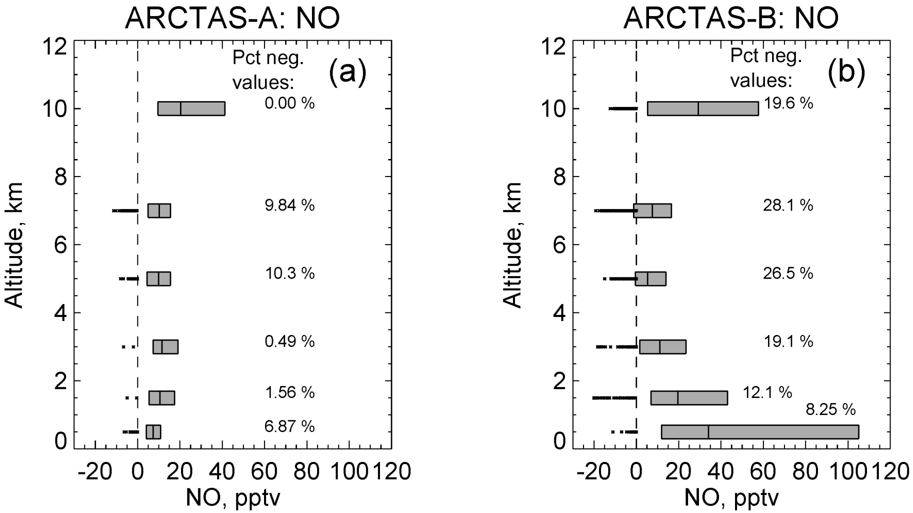

Fig. 2. Range of NO observations during **(a)** ARCTAS-A and **(b)** ARCTAS–B for 1-min averages of NO. Bars show the inner 50th percentile range (25–75 %) and vertical lines within bars indicate the median values. Negative values are shown with black points to the left of the dashed line that indicates zero. The percentage of negative values is indicated at each altitude bin.

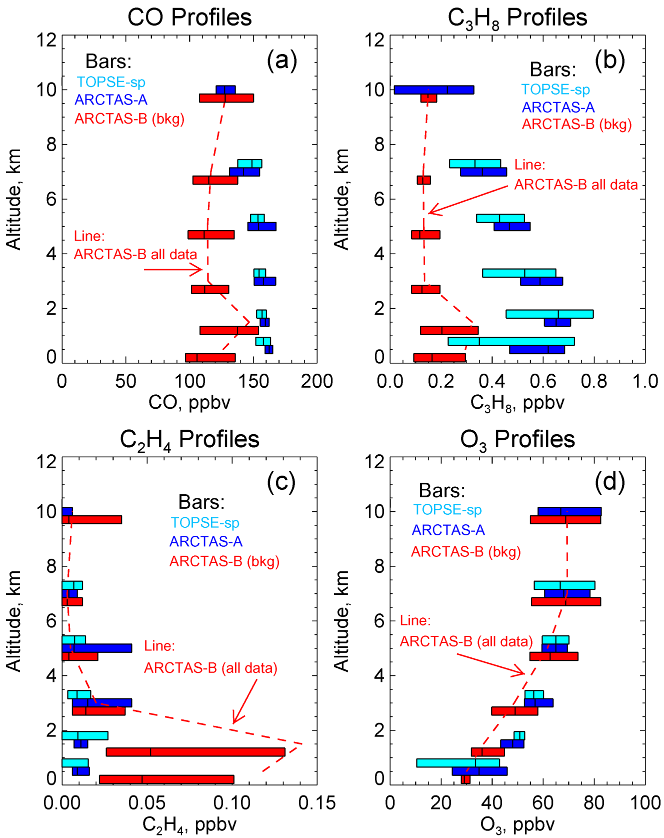

Fig. 3. Profiles of measurements of **(a)** CO, **(b)** C_3H_8 **(c)** C_2H_4 and **(d)** O_3 during ARCTAS and during TOPSE-sp. Bar plots are as described in Fig. 2. Data for ARCTAS-B shown by the bar plots exclude values identified as within fresh plumes. The dashed lines show the median profile for ARCTAS-B when all data are considered (including fresh plumes).

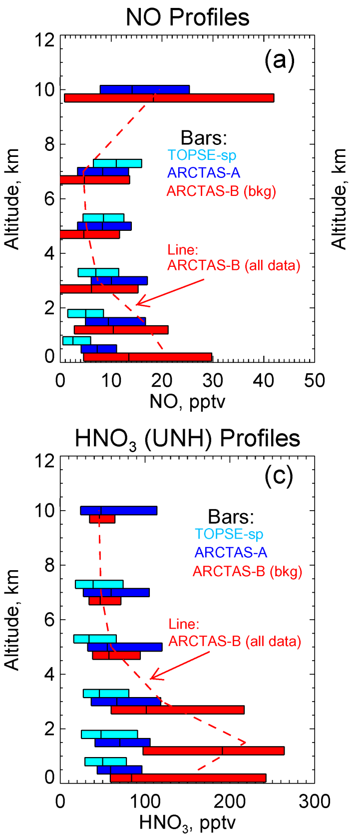

Fig. 4. Profiles of **(a)** NO, **(b)** NO/NO_2 and **(c)** HNO_3 during ARCTAS and during TOPSE-sp. Bar plots and dashed lines are as described in Fig. 3.

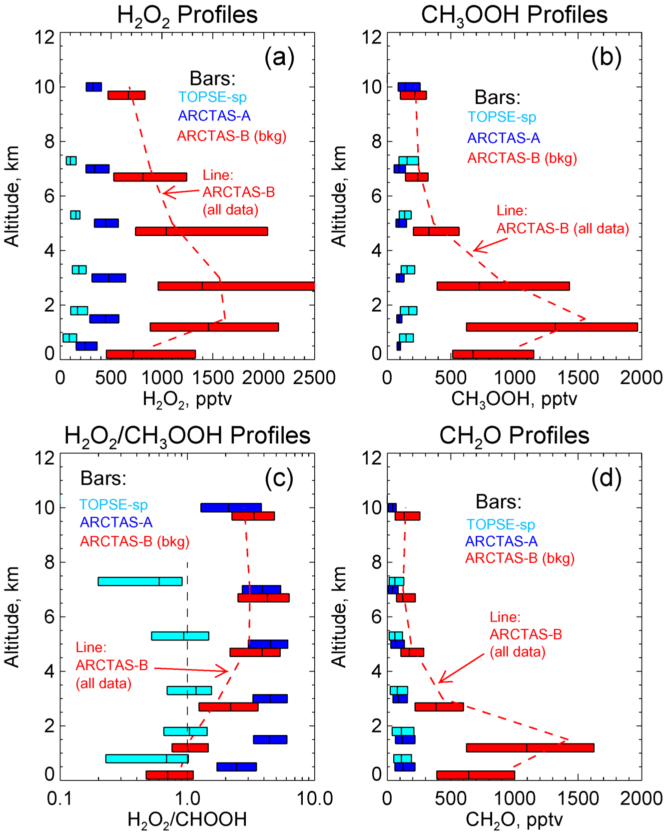

Fig. 5. Profiles of **(a)** H_2O_2, **(b)** CH_3OOH, **(c)** H_2O_2/CH_3OOH, and **(d)** CH_2O during ARCTAS-A and -B and during TOPSE-sp. Bar plots and dashed lines are as described in Fig. 3.

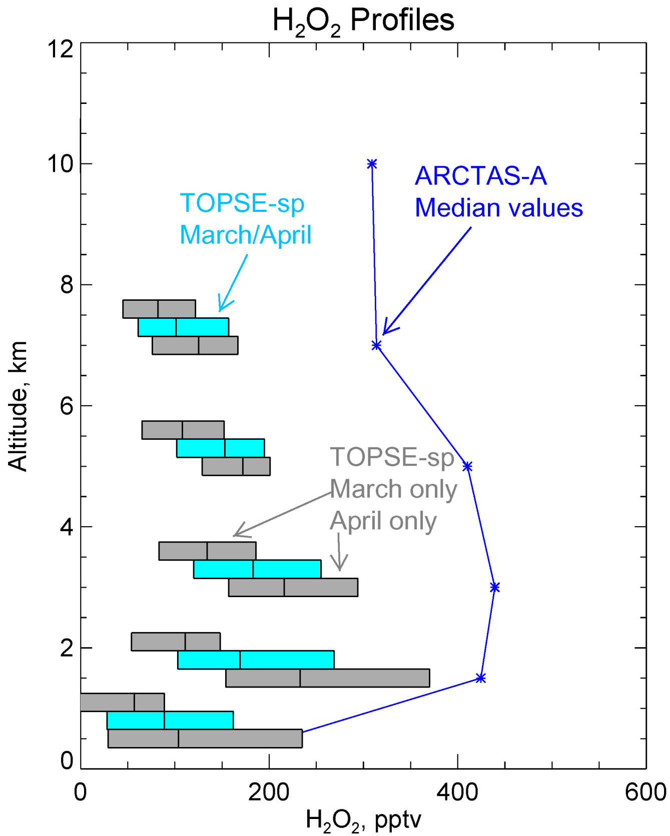

Fig. 6. Median observations of H_2O_2 during ARCTAS-A, and during TOPSE-sp, using combined March/April data versus March only and April only.

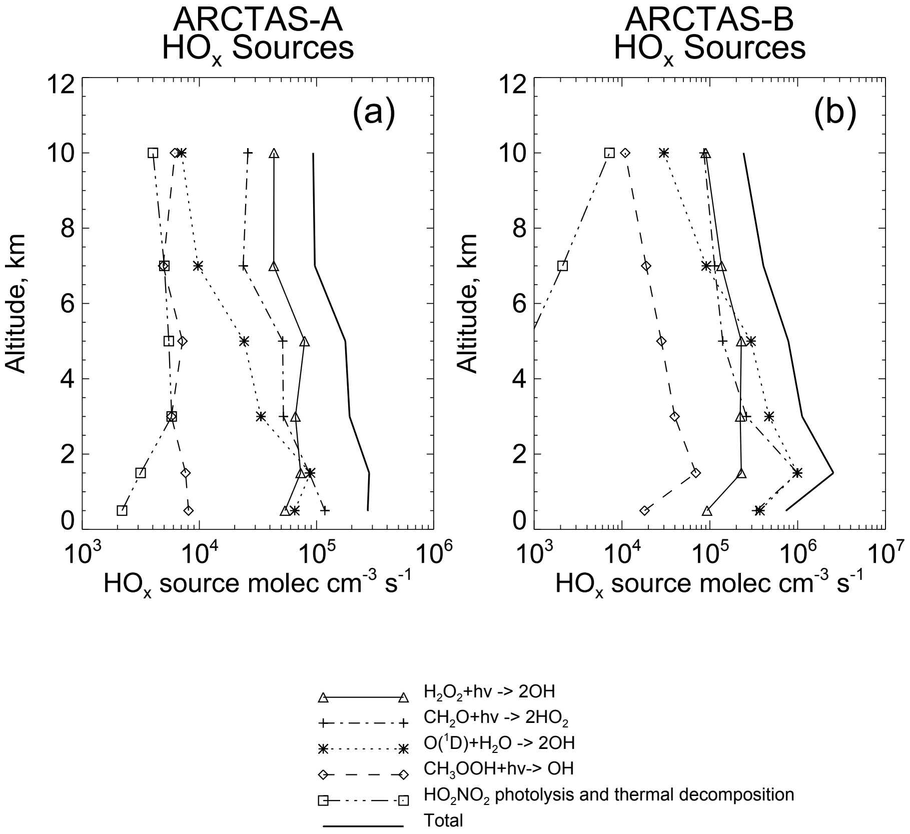

Fig. 7. Gross HO$_x$ production during **(a)** ARCTAS-A and **(b)** ARCTAS-B.

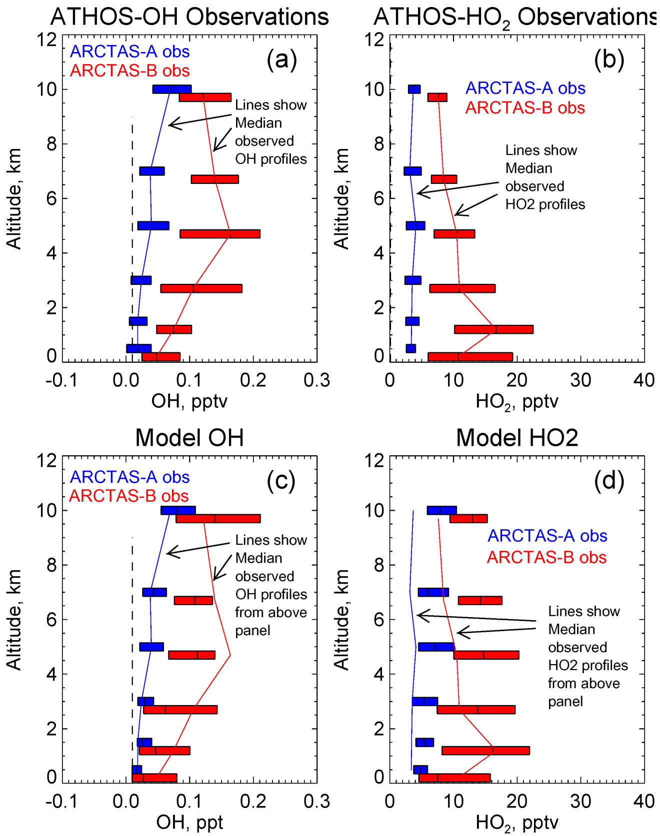

Fig. 8. Profiles of observed **(a)** OH and **(b)** HO_2 and of model-predicted **(c)** OH and **(d)** HO_2 during ARCTAS. Bar plots are as described in Fig. 2. The lines indicate the median observed profiles of OH and HO_2.

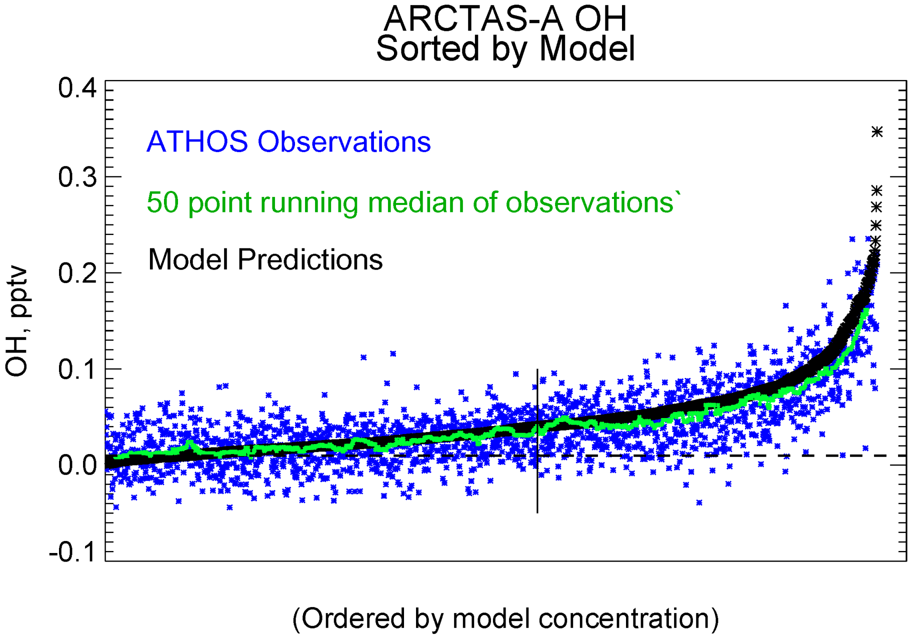

Fig. 9. Observed (blue) and model-predicted (black) concentration pairs of OH during ARCTAS-A sorted by increasing model concentration. The green line shows a 50 point running median of observations along the sorted values.

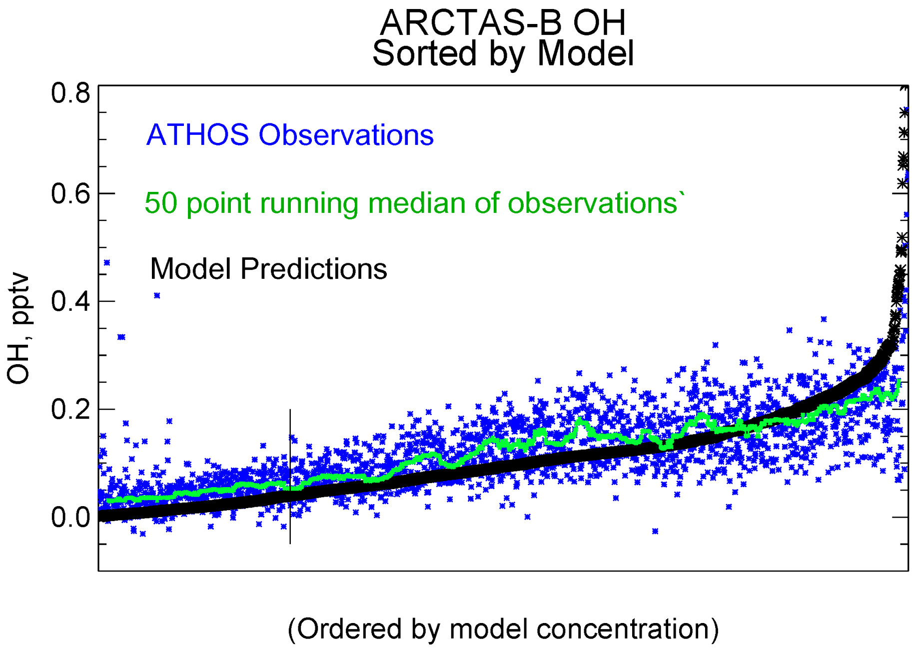

Fig. 10. Observed (blue) and model-predicted (black) concentrations pairs of OH during ARCTAS-B sorted by increasing model concentration. The green line shows a 50 point running median of observations along the sorted values.

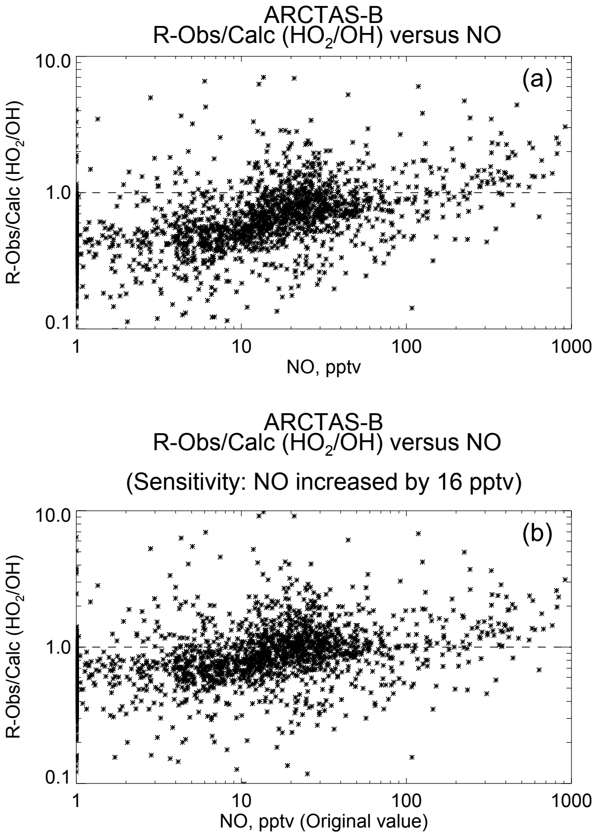

Fig. 11. Observed-to-calculated ratio of the HO_2/OH partitioning during ARCTAS-B as a function of NO. Results from the standard model simulation are shown in **(a)** and results when NO is universally increased by 16 pptv are shown in **(b)**.

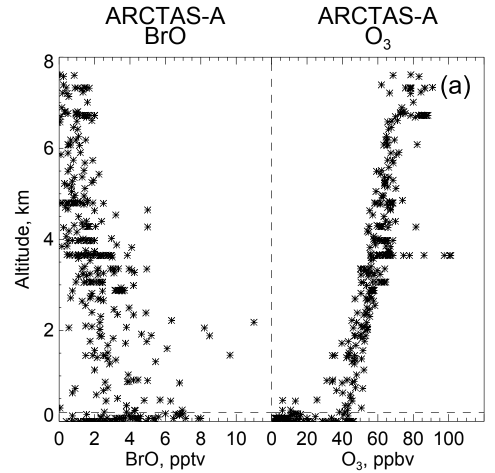

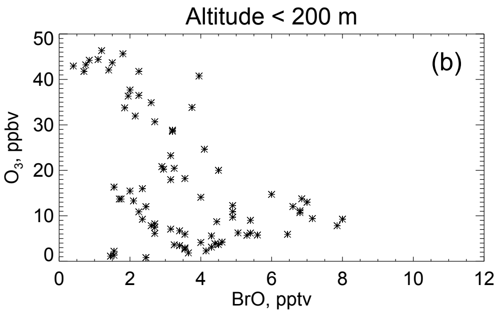

Fig. 12. Observations of BrO and O_3 during ARCTAS-A. **(a)** shows observed altitude profiles of BrO and O_3 and **(b)** shows the correlation between BrO and O_3 in the lowest 200 m.

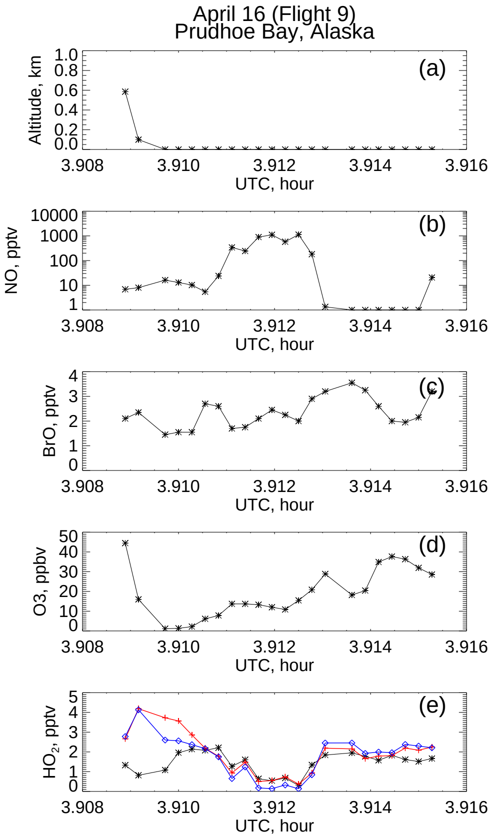

Fig. 13. Case study for impact of bromine on April 16. Observed time series are shown for **(a)** Altitude, **(b)** NO, **(c)** BrO, and **(d)** O_3. Observations of HO_2 are shown in panel **(e)** along with model predictions of HO_2 with and without BrO chemistry.

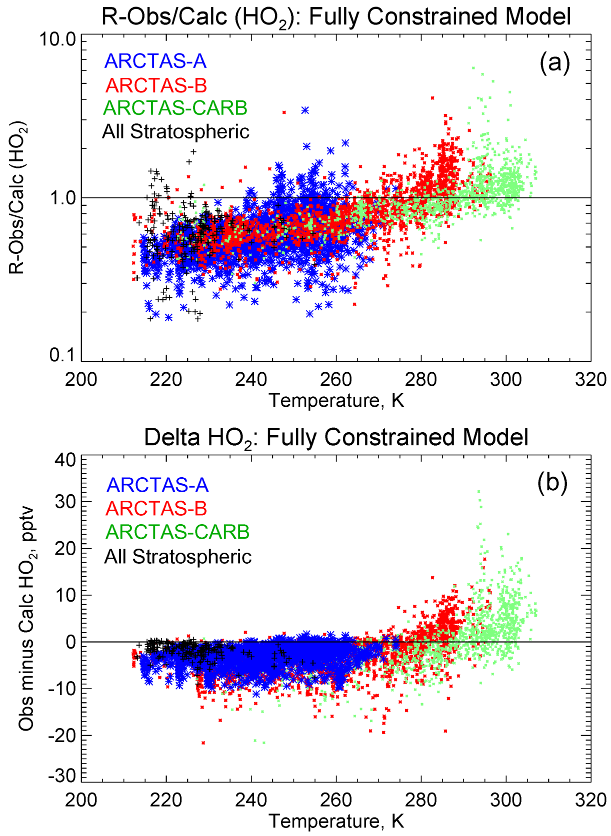

Fig. 14. Model predicted and observation comparisons for HO_2 as a function of temperature. **(a)** shows R-Obs/Calc (HO_2) for ARCTAS-A, -B and -CARB and **(b)** shows the difference between observations and model predictions for HO_2 as a function of temperature.

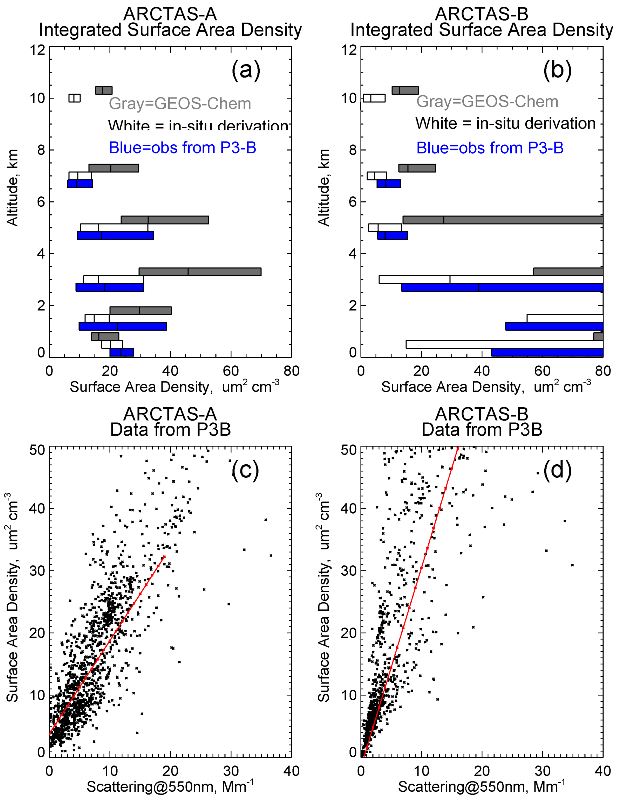

Fig. 15. Integrated surface area density (SAD) and scattering@550 nm during ARCTAS. Altitude profiles of SAD are shown for **(a)** ARCTAS-A and **(b)** ARCTAS-B. Bars show values of SAD obtained from P3-B observations, from derivations using a correlation to DC-8 observations of scattering@550 nm, and from calculations using the GEOS-Chem model. Bar plots are as described in Fig. 2. The correlation between measurements of SAD and scattering@550 nm from the P3-B are shown for **(c)** ARCTAS-A and **(d)** ARCTAS-B.

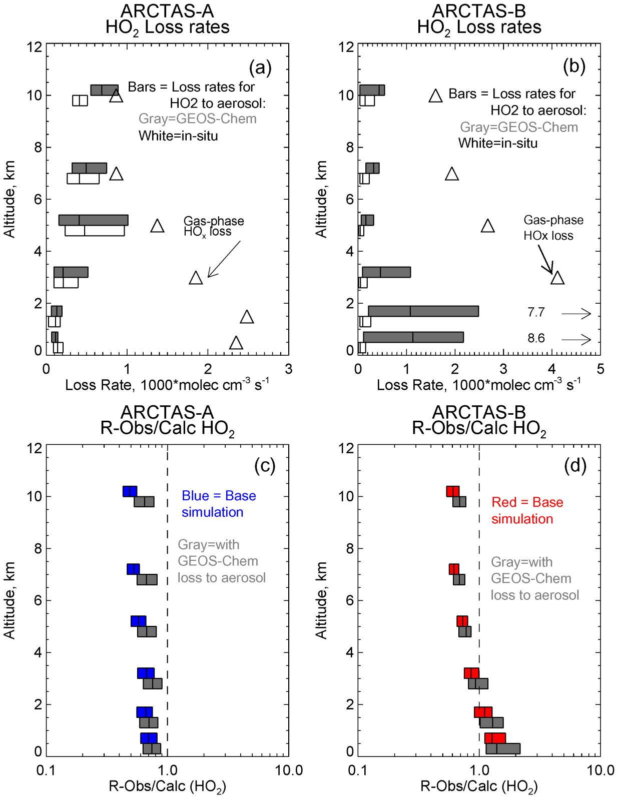

Fig. 16. Impact of including a heterogeneous loss rate of HO_2 to aerosol on predictions of HO_2. Altitude profiles of the loss rate of HO_2 to aerosol calculated in GEOS-Chem and from using in-situ observations as described in Sect. 4.3.4 are shown for **(a)** ARCTAS-A and **(b)** ARCTAS-B. Predictions of the gas-phase loss of HO_2 using the LaRC box model and in-situ observations are shown for comparison. Altitude profiles of the observed-to-calculated ratios of HO_2 from simulations that do and do not include the heterogeneous loss of HO_2 to aerosol are shown for **(c)** ARCTAS-A and **(d)** ARCTAS-B.

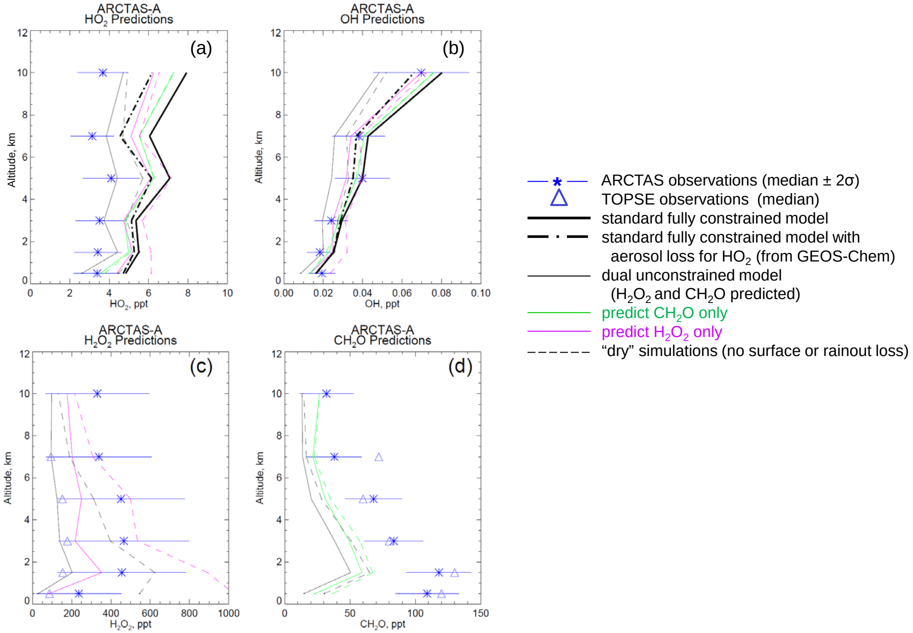

Fig. 17. Altitude profiles for observations and model predictions of **(a)** HO_2, **(b)** OH, **(c)** H_2O_2 and **(d)** CH2O during ARCTAS-A, with model predictions from several different permutations of the LaRC box model. Asterisks show the median observations, and the associated horizontal blue lines indicate the 2σ uncertainty in the observation. Median observations of H_2O_2 and CH_2O from TOPSE-sp are shown with triangles in **(c)** and **(d)**.

ACPD
12, 9377–9450, 2012

Title Page
Abstract
Introduction
Conclusions
References
Tables
Figures
◀|
|▶
◀
▶
Back
Close
Full Screen / Esc
Printer-friendly Version
Interactive Discussion

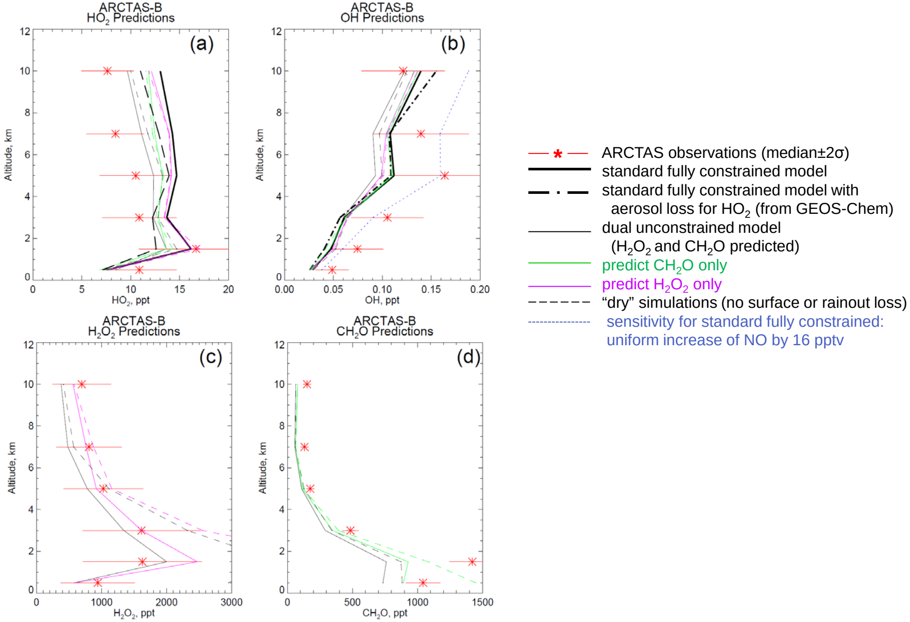

Fig. 18. As in Fig. 17, but for ARCTAS-B.

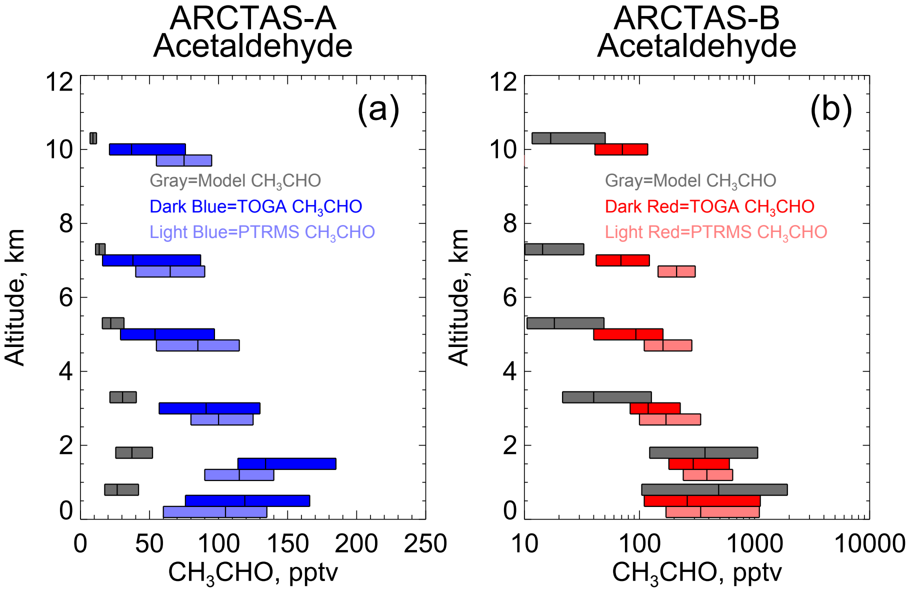

Fig. 19. Altitude profiles of observations and model predictions of acetaldehyde during **(a)** ARCTAS-A and **(b)** ARCTAS-B. Bar plots are as described in Fig. 2.

Title Page

Abstract Introduction

Conclusions References

Tables Figures

◀▮ ▶▮

◀ ▶

Back Close

Full Screen / Esc

Printer-friendly Version

Interactive Discussion

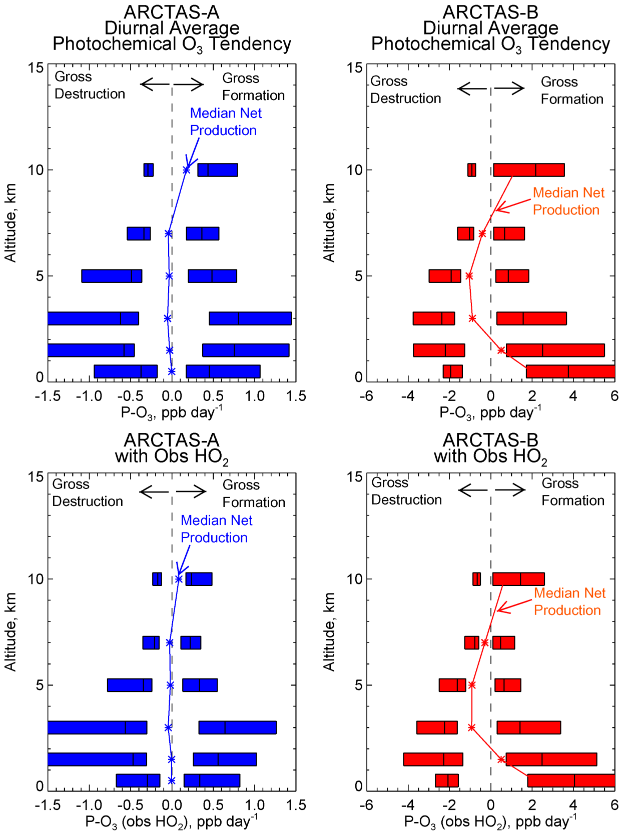

Fig. 20. Altitude profiles of diurnally averaged model calculated gross formation and destruction and net production of O_3 during **(a)** ARCTAS-A and **(b)** ARCTAS-B. Bar plots are as described in Fig. 2. Figures **(c)** and **(d)** are for the diurnally averaged gross formation and destruction and net production of O_3 using observed HO_2 rather than model predictions.

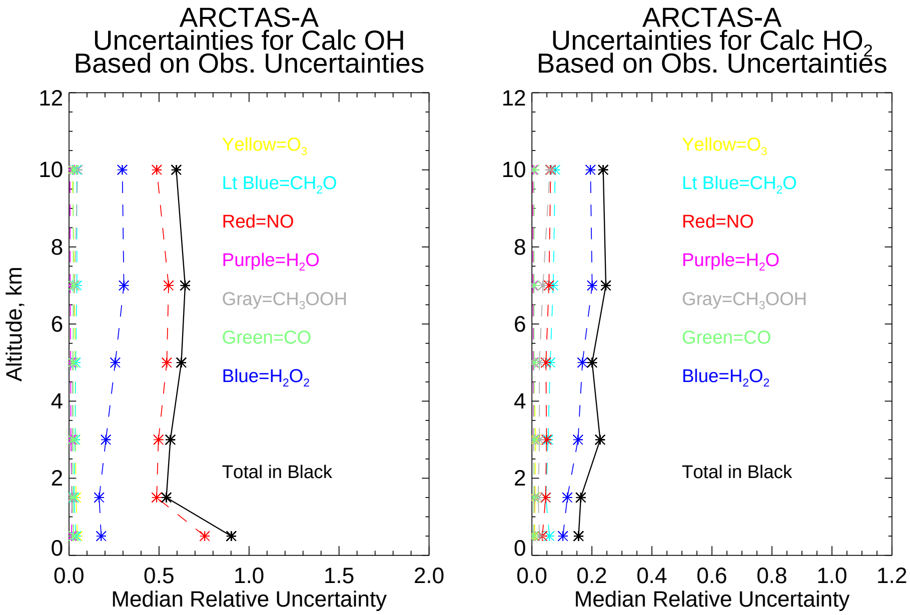

Fig. A1. Altitude profiles of the median relative uncertainty in prediction of **(a)** OH and of **(b)** HO_2 during ARCTAS-A that is due to the uncertainty in observations of constraining species.

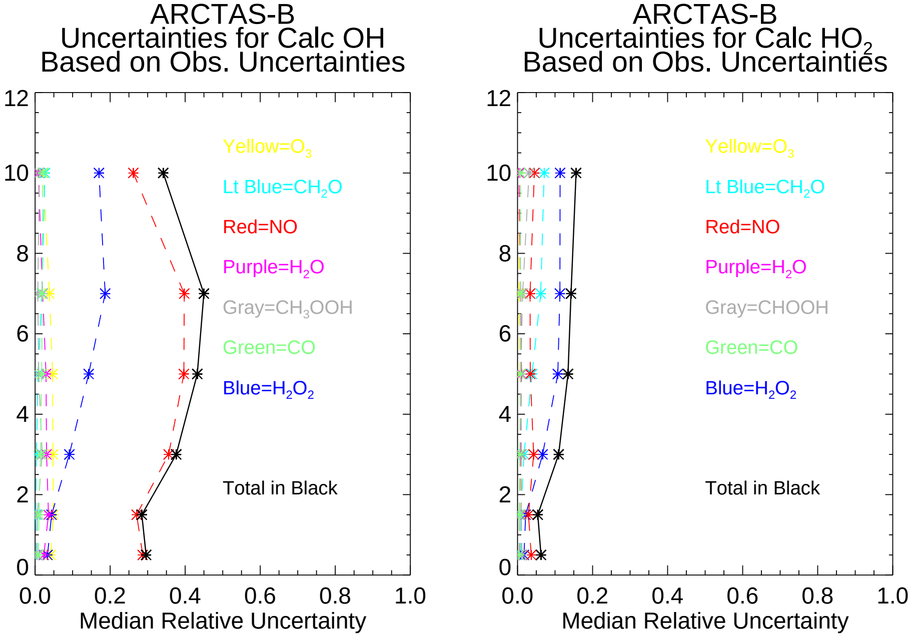

Fig. A2. As for Fig. A1, but for ARCTAS-B.